Haberland, C., Riedbrock, A., Lange, D., Bataille, K., Dahm, T. (2009): Structure of the seismogenic zone of the southcentral Chilean margin revealed by local earthquake traveltime tomography. - Journal of Geophysical Research, 114, B01317

DOI: 10.1029/2008JB005802

Structure of the seismogenic zone of the South-Central Chilean margin revealed by local earthquake travel time tomography

Christian Haberland,[1,2] Andreas Rietbrock,[3] Dietrich Lange,[2,4,5] Klaus Bataille,[6] and Torsten Dahm[4]

Christian Haberland, Deutsches GeoForschungsZentrum (GFZ), Telegrafenberg, 14473 Potsdam, Germany (haber@gfz-potsdam.de)

Andreas Rietbrock, Department of Earth and Ocean Sciences, University of Liverpool, UK, (A.Rietbrock@liverpool.ac.uk)

Dietrich Lange, Bullard Laboratories, University of Cambridge, UK, (dl385@cam.ac.uk)

Klaus Bataille, Dept. Ciencias De La Tierra, Universidad de Concepción, Chile, (bataille@udec.cl)

Torsten Dahm, Institute of Geophysics, University of Hamburg, Germany, (Torsten.Dahm@zmaw.de)

[1]Deutsches GeoForschungsZentrum

Abstract. We use travel time data of local earthquakes and controlled sources observed by a large, temporary, amphibious seismic network to reveal the anatomy of the South-Central Chilean subduction zone (37° - 39° S) between the trench and the magmatic arc. At this location the giant 1960 earthquake (M=9.5) nucleated and ruptured almost 1000 km of the subduction mega-thrust. For the 3-D tomographic inversion we used 17,148 P-wave and 10,049 S-wave arrival time readings from 439 local earthquakes and 94 shots. The resolution of the tomographic images was explored by analysing the model resolution matrix and conducting extensive numerical tests. The downgoing lithosphere is delineated by high seismic P-wave velocities. High

(GFZ), Potsdam, Germany

[2]Institute of Geosciences, University of Potsdam, Germany

[3]Department of Earth and Ocean Sciences, The University of Liverpool, UK

[4]Institute of Geophysics, University of Hamburg, Germany

[5]Bullard Laboratories, University of Cambridge, UK

[6]Dept. Ciencias De La Tierra, Universidad de Concepción, Chile

v_p/v_s ratio in the subducting slab reflects hydrated oceanic crust and serpentinized uppermost oceanic mantle. The subducting oceanic crust can be traced down to a depth of 80 km as indicated by a low velocity channel. The continental crust extends to approximately 50 km depth near the intersection with the subducting plate. This suggests a wide contact zone between continental and oceanic crust of about 150 km potentially supporting the development of large asperities. Eastward the crustal thickness decreases again to a minimum of about 30 km depth. Relatively low v_p/v_s at the base of the forearc does not support a large-scale serpentinization of the mantle wedge. Offshore, low v_p and high v_p/v_s reflect young, fluid-saturated sediments of forearc basins and the accretionary prism.

1. Introduction

The largest earthquakes on earth are generated along the shallow portions of subduction zones where the upper and lower plates are in contact over long time-scales thus accumulating large stresses across the fault. The coseismic slip along these thrust planes during large earthquakes seems to be highly nonuniform, and patches of high slip, known as asperities, alternate with regions of less slip [*Lay and Kanamori*, 1981]. However, the physical meaning of these asperities and the processes involved in the nucleation and development of large and very large earthquakes are still poorly understood.

While properties of the lower plate such as temperature, age, or roughness were proposed as the main factors for controlling the seismogenic behaviour at the plate interface for a long time, properties and structure of the upper plate came into focus recently [e.g., *McCaffrey*, 1993; *Collot et al.*, 2004; *Song and Simons*, 2003; *Fuller et al.*, 2006]. In particular the structure of the continental crust (i.e., crustal thickness) and the state and properties of the mantle wedge beneath the crustal forearc were identified to be important parameters since they imply significant consequences for the rheological properties of the interface between the upper and lower plates, for the extent of the seismogenic zone, and finally for the occurrence of large earthquakes. It had been proposed that the lower or down-dip end of the seismogenic zone is either controlled by the depth at which the temperature at the plate interface reaches 350° to 450° C or where the crust mantle boundary intersects with the subducting plate [*Hyndman and Wang*, 1993; *Hyndman et al.*, 1997]. Morover, it had been proposed that the updip limit of the 'minor' or background seismicity at the plate interface is spatially coincident with the updip limit of the rupture zone of large earthquakes inferred from the aftershock distribution [*Byrne et al.*, 1988]. Recently the structure of a number of subduction zones had been successfully investigated by active and passive seismic investigations (Vancouver, Cascadia, Japan, Costa Rica) [e.g., *Eberhart-Phillips et al.*, 2005; *Reyners et al.*, 2006; *Ramachandran et al.*, 2006; *Newman et al.*, 2002; *DeShon et al.*, 2006; *Eberhart-Phillips et al.*, 2006].

The main issues we address are: Are there structures in the continental and/or oceanic lithosphere supporting the nucleation and/or development of large earthquakes? What are the characteristics of and the processes within the seismogenic zone?

In order to decipher the structure of the South-Central Chilean subduction zone and to infer the processes involved we analyse detailed seismic velocity models and high-precision locations of the 'minor' subduction zone earthquakes occurring in the interseismic period. In particular, the mapping of the ratio of seismic P and S-wave velocities (v_p/v_s) has the potential to resolve the presence of fluids and to infer the physical state of the material [e.g., *Husen and Kissling*, 2001]. Data are provided by an exceptionally dense, temporary, amphibious seismic network.

2. Tectonic setting, regional geology, and seismicity

The study area is located between 37° and 39° S at the South-Central Chilean continental margin. Here the oceanic Nazca plate subducts obliquely (ENE) at a convergence rate of 6.6 cm/y beneath the South American continent [e.g., *Angermann et al.*, 1997]. The Nazca plate between 39° and 37° S has an age of between 25 to 30 Ma [*Tebbens and Cande*, 1997].

This southern part of the Chilean margin is considered to be strongly coupled [*Uyeda and Kanamori*, 1979]. Giant earthquakes repeatedly occur along the margin with a recurrence rate of several centuries [*Cisternas et al.*, 2005]. The last such earthquake happened in 1960 when the worldwide largest instrumentally observed earthquake (Mw=9.5) ruptured an approximately 1000 km long region thus producing a circumpacific tsunami [*Plafker and Savage*, 1970; *Barrientos and Ward*, 1990; *Cifuentes*, 1989]. North of 38°30' S most of the 'minor' or background seismicity is concentrated in the coastal region and forms a prominent earthquake cluster in the Arauco region (Figure 1). The 1960 earthquake nucleated here. South of 38°30' S seismicity diminishes. Most of the earthquakes in this segment down to Chiloé island are situated at the Peru-Chile trench.

The continental margin between 36° and 42° S can be subdivided in a series of trench-parallel trending morphotectonic units (Figure 2). It has evolved as an active margin since the Pennsylvanian (300 Ma) and exhibits a rather complex internal architecture reflecting it's eventful history. Carboniferous to Triassic metasediments of the so-called 'Eastern series' originating from former passive margin sediments and intruded by late Paleozoic to Triassic arc granitoids (coastal batholith), form the Coastal Cordillera north of 38° S. South of 38° S Permo-Triassic metasediments of the 'Western Series' (paleo-wedge) predominate in the Coastal Cordillera and also form the deeper part of the continental shelf in the study area [*Aguirre et al.*, 1972]. The prominent, NNW-SSE striking, mylonitic Lanalhue shear zone (LSZ) separates these two series and is assumed to be a major dissection of the Paleozoic margin architecture [e.g., *Glodny et al.*, 2006]. Seismicity along this fault zone indicates ongoing activity [*Haberland et al.*, 2006]. A series of sedimentary forearc basins developed in the continental shelf area at Cretaceous to Holocene time [*Mordojovich*, 1981]. Parts of these basins were uplifted during the Quaternary and emerge today in the Arauco peninsula and Mocha and Santa Maria islands above sea level [*Melnick et al.*, 2006; *Melnick and Echtler*, 2006b]. A small accretionary prism at the toe of the continental forearc indicates the recent (1-2 Ma) accretionary mode of the continental margin, which, however, was not consistently maintained throughout the Neogene. In fact, it is assumed that today's morphology is predominantly influenced by subduction-erosion processes [*Bangs and Cande*, 1997].

To the east, the Central Depression (CD, or Longitudinal Valley) is a sedimentary depository with up to 2000 m thick sedimentary layers. The easterly adjacent Principal Cordillera is the location of the magmatic arc since the Jurassic. Recent volcanic arc edifices up to 3700 m high formed on top of the North-Patagonian batholith and Cenozoic sedimentary and volcanic intra-arc basins.

The region of the Arauco peninsula is a major subduction zone segment boundary. Recently *Wang et al.* [2007] presented evidence that a large crustal forearc sliver bounded to the east by the Liquine-Ofqui fault zone (LOFZ), a 1000 km long, trench-parallel, intra-arc shear zone, moves northwards as a result of the oblique subduction of the Nazca plate [see e.g. also *Lange et al.*, 2008, and Figure 1].

3. Data

We used data recorded by the temporary, amphibious TIPTEQ network which was in operation in south-central Chile between November 2004 and October 2005 [*Rietbrock et al.*, 2005; *Haberland et al.*, 2006]. It covered the entire forearc between 37° and 39°S (see Figure 3). Between October 2004 and January 2005 it consisted of 70 PDAS and REFTEK data loggers, running in continuous mode at sample rates of 50 and 100 sps respectively. All instruments were replaced by EDL dataloggers between February and June 2005 and an additional 50 EDL stations were deployed to increase the station density.

A reduced number of 20 land stations were in operation from July through October 2005. All stations were equipped with short-period three-component seismometers. Between mid-February and October 2005 10 wide-band ocean bottom seismometers (OBS) and hydrophones (OBH) complemented the network on the offshore forearc. Average station spacings were very small in the center (around 7 km) and larger in the outskirts of the region of interest (40 km). See Table 1 for network details.

3.1. Earthquake data

On average the network observed 2 to 3 local events per day. Events were detected by applying an automatic STA/LTA trigger to the individual station data followed by a temporal coincidence check across all network stations. Additional events were detected by visual inspection of the continuous data by an analyst. Onset times of the compressional (P) and shear (S) waves were manually picked with the GIANT/PITSA software code [*Rietbrock and Scherbaum*, 1998].

Data quality was generally high, resulting in 15,734 P-wave and 10,049 S-wave observations of 439 local events which were used for the tomographic inversion (see Figure 4). High quality S-wave arrivals particularly in the coastal ranges were recorded. Quality of the picks was associated according to the apparent pick uncertainty, with 0 being the highest quality (pick uncertainty +- 0.02 s) to 2 being the lowest used in the inversion (pick uncertainty +- 0.2 s).

The land stations provided most of the travel-time observations (15,453 P and 9,989 S-wave observations), a smaller amount of data was provided by the 6 working OBS/OBH stations (281 P and 60 S-wave picks). See Figure 5 for data example of onshore and offshore data.

3.2. Controlled source data

During the accompanying controlled source seismic experiment 104 chemical explosions (75 - 300 kg) were shot in up to 25 m deep boreholes during January 2005 [*Groß et al.*, 2008]. Absolute shot times and coordinates were determined using GPS (see Figure 4). The shots were observed by up to 70 stations of the land network during the first phase of the deployment (see above). The observation distances were up to 100 km. For the tomographic study we used observations of 94 shots which had at least 10 P-wave picks. S-waves from the shots were not observed. This resulted in 1,414 P-wave picks aditionally used in the inversion which constrained the velocity model in the uppermost part, in particular in the vicinity of the seismic line.

4. Method - 3-D tomographic inversion

We apply the well established and widely used inversion code SIMUL2000 [*Thurber*, 1983, 1993; *Evans et al.*, 1994; *Eberhart-Phillips*, 1986a; *Eberhart-Phillips and Michael*, 1998]. In the damped least-squares inversion the three-dimensional velocity structure (v_p and v_p/v_s) is calculated from the observed traveltimes. Due to usually reduced quality and quantity of the S-wave data, the code inverts for the v_p/v_s ratio instead of an independent v_s model. Efficient pseudo-bending is used for the raytracing and the calculation of synthetic traveltimes [*Um and Thurber*, 1987]. The velocity models are defined on the intersections of a rectangular grid. Between the nodes, linear B spline interpolation yields a continuous spatial variation of the parameters. Additionally, the inversion for individual station corrections can be included. The parameters of the raytracer, in particular the characteristic length scales used in the raytracing algorithm and the parameter controlling the rotation angles of the plane of the ray, were adjusted based on comparison of synthetic travel times with results obtained by Finite Difference simulations [*Podvin and Lecomte*, 1991; *Tryggvason and Bergman*, 2006].

Following common practice we applied a staggered inversion scheme starting with inversions for a 1-D model, followed by inversions for coarse 2-D, fine 2-D and finally the fine 3-D model. Due to the highly asymmetric, 2-D velocity structure of the shallow part of subduction zones, the deviation from the 1-D velocity structure is considerable. The use of a staggered approach assures that the velocity values of poorly resolved nodes will not be allowed to deviate significantly from the starting model therefore avoiding complicated artifacts in the 3-D inversion. The starting 1-D velocity model (see Figure 6) used is the previously calculated 'minimum 1-D model' [*Haberland et al.*, 2006] obtained from inversion by using the program code VELEST [*Kissling et al.*, 1994]. For the v_p/v_s starting model in the coarse 2-D inversion we assumed a constant value of 1.77 based on Wadati diagram analysis. In subsequent inversions we used the previously calculated v_p and v_p/v_s models (or its interpolated representations, respectively) as starting models. Relocation of the hypocenters is part of each inversion step.

For the tomographic inversion we only used events with at least 10 P and 4 S-wave observations of high quality [*Haberland et al.*, 2006]. For establishing the 2-D velocity models we only used travel time data of earthquakes within the network (largest azimuthal gap of the stations (GAP) smaller than 180°). The broad-scale structure of the subduction zone is set during 2-D inversion, providing a more accurate velocity model to constrain events in and outside of the network coverage. We relocated all earthquakes within the 2-D model and subsequently relaxed the GAP criterion during 3-D inversion using all raypaths from events up to a GAP of 210° to yield better sampling of the volume of interest. In order not to remove signal in the data, we accepted travel time readings with initial residuals of up to 3 s in the 2-D inversions. However, for the final 3-D inversion we excluded data with initial residuals of larger than 1 s in order to remove outliers. The final dataset used in the 3-D inversion consists of events which have typically between 10 and 40 P-wave observations and between 10 and 25 S-wave observations per event. However, 15% of all earthquakes used have more than 100 observations.

In the coarse 2-D velocity model horizontal (W-E) grid node spacing was 15 km in the center of the network, and 10 km in the vertical direction down to a depth of 70 km plus an additional node plane at 5 km depth (Figure 4). The fine grid had horizontal (W-E) spacing of 15 km and a 5 km spacing in depth. The 3-D model had similar spacings in depth and W-E direction as the fine 2-D model, together with a horizontal spacing of 20 km in N-S direction. These values were derived after extensive tests and represent a good balance between desired spatial resolution and available seismic data. East of 72.6° W and below 30 km depth we linked each two vertically adjacent nodes together in order to account for predominant vertical raypaths and generally less ray coverage. In the inversion all nodes linked together are treated as one node thus mimicking a coarser parametrization in regions with reduced resolution which further stabilizes the model in these regions [*Thurber and Eberhart-Phillips*, 1999].

In the well resolved regions of the model the minimal spatial resolution is given by the grid spacing used. In order to model the expected gently dipping structures (i.e., the downgoing plate) accurately with the regular, rectangular grids we used a fine grid spacing (see above). To remove any artifacts due to node configuration we calculated additional inversions with horizontally shifted grids (shifted by 3 and 7 km, which is less than the grid spacing used), and averaged the resulting models, a procedure regularly used in teleseismic tomography [e.g., *Foulger et al.*, 2000]. This procedure applied to both the 2-D and 3-D models provides smooth and robust final models on the one hand and accurate imaging of dipping structures on the other.

Damping in all inversions was chosen after inspection of the so-called trade-off curve resulting in damping values which minimize the data variance at a moderate model variance [*Eberhart-Phillips*, 1986b]. This yields relatively smooth and simple models that explain the data reasonably well. For determining the appropriate damping of the v_p model we performed one-step inversions with varying v_p damping and a fixed v_p/v_s ratio. For the subsequent determination of the damping of the v_p/v_s model we fixed the v_p model damping according to the previously obtained value. Damping for the stations corrections was set to a relatively high value such that the resulting corrections do not show regional trends extending over several neighboring stations, which would better be accounted for by regular shallow velocity nodes. Therefore, they do not exceed 0.05 s. The reference station (no correction) was station A409 in the coastal range (same as in the VELEST inversion; see Figure 3).

The final inversion yields a significant reduction of the variances for both the P and S-wave data. The P-wave data variance reduction is 81% compared to the 1-D model and the S-wave data variance reduction is 71 % compared to the homogeneous model (v_p/v_s =1.77). Important inversion parameters and the data variances of the particular steps within our staggered inversion scheme are summarized in Table 2.

5. Resolution

Due to the irregular distribution of sources and receivers, the subsurface structure is resolved with spatially varying quality. To assess the resolution of the obtained velocity models we performed synthetic restoring test and inspected the model resolution matrix.

5.1. Model resolution Matrix

The model resolution matrix (MRM) provided by the inversion algorithm contains information on how well each inversion parameter is resolved and how much smearing into adjacent nodes is present. Well resolved nodes have large diagonal elements and small off-diagonal elements. Smearing can be visualized both in terms of quantity and quality by inspection of the spread function (SF, *Toomey and Foulger* [1989]) and of the shape of the resolution kernels.

Figure 7 shows these parameters for the v_p nodes and v_p/v_s nodes along five west-east depth sections. Large diagonal elements of the MRM, small SF values and close contour lines of the 70% resolution kernel suggest that a large volume of the central part of the model is well resolved due to many crossing raypaths. Toward the periphery the diagonal elements decrease quickly and SF values climb above 3.5 indicating fading resolution. Regions with predominantly subparallel raypaths show considerable smearing in the direction of the rays. This is the case in the eastern part of the model where predominantly vertical smearing is present due to the lack of horizontal raypaths.

The offshore forearc is poorly resolved. This is mainly due to the limited number of events and the sparse station coverage in this part of the study area. Moreover, due to low seismic velocities in the offshore forearc wedge, rays travel within the fast subducting plate and therefore yield a reduced ray coverage of the wedge itself (see Figure 4).

The subhorizontally elongated contours in the coastal area west of approximately 74° W indicate the resulting horizontal smearing in this part of the model.

SF values of the v_p/v_s model are comparable to the values of the v_p model (see Figure 7) and the close contour lines of the MRM indicate good resolution. This is particularly true for the deeper parts of the model where we expect the subducting plate. However, vertical v_p/v_s smearing appears larger than the v_p smearing.

5.2. Synthetic recovery tests

In the recovery tests we designed synthetic velocity models (both v_p and v_p/v_s), calculated traveltimes for the actual source and receiver geometry, and added random noise to the synthetic traveltimes. We then inverted these synthetic traveltimes in the same way as the real data (2-D). Comparison of the input model and the recovered model provides another assessment of model resolution.

Instead of using synthetic models with the same parametrisation (i.e. relatively coarse regular grid with spacing in the order of 5 to 15 km) as used in the tomographic inversions of the real data we used finely discretized models with a small grid spacing of 500 m, and applied 3-D finite difference simulation [*Podvin and Lecomte*, 1991; *Tryggvason and Bergman*, 2006]. This allows us to investigate the capability and limitations of our tomographic inversions for imaging small, thin and inclined structures and strong gradients such as a few-kilometers thin oceanic crust or the inclined mega-thrust plane. In addition, we can test the performance of the pseudo-bending raytracing used in the inversions.

The v_p structure of the continental plate of the synthetic background model is based on the results of previous work [*Krawczyk et al.*, 2006; *Bohm*, 2004] and of this study. We introduced a 7 km thick anomaly reflecting the subducting crust with values for v_p

consistent with seismic sea floor studies and laboratory data [e.g., *Raitt*, 1956; *Raitt et al.*, 1969]. Mantle velocities reflect the global average [e.g., *Montagner and Kennett*, 1996].

The amount of normally distributed random noise added to the synthetic traveltimes was selected to reflect the quality associated with each real observation: for highest quality readings (weight 0) we added random noise with a standard deviation of 0.05 s, increasing to 0.15 s for phases of lowest quality (weight 2).

We tested several models, in particular v_p/v_s models. Within the minimal spatial resolution given by the grid spacing the synthetic v_p model is very well resolved in the ray-covered region (Figure 8 A). Even in less resolved regions no significant artifacts are introduced. The absolute values of v_p anomalies in the continental forearc crust between 74.2° and 71.8° W and the mantle wedge are reproduced within an accuracy of $+-$ 2%. As anticipated, the recovery of structures smaller than the grid spacing is poor. However, even within the thin oceanic crust above 50 km depth, the v_p values are only slightly overestimated (by approximately 5%). Large-scale v_p/v_s anomalies within the subducting lithosphere are also well resolved particularly with respect to their upper bound (Figure 8 B & C; upper bound of red and blue anomalies). The absolute values of v_p/v_s in the upper part of the anomalies are reproduced well with an accuracy of $+-$ 2%. Furthermore, variations of the v_p/v_s ratio along the subducting slab seem to be reasonably well resolved (Figure 8 B; eastern bound at 72.8° W). The lower bound of the slab-anomalies could not be resolved. Large-scale v_p/v_s anomalies within the continental forearc as one might expect for hydrated and/or fluid saturated regions of the mantle wedge and/or the marine forearc are well reproduced (Figure 8 D). Aside from some smearing, the absolute values of these synthetic anomalies are also attained by the inverted model.

6. Results and discussion

The 2-D and 3-D tomographic models show the highly asymmetric velocity structure expected for an easterly-vergent subduction zone setting. The 2-D model is shown in Figure 9, the 3-D model is presented in various vertical and horizontal sections (Figure 10 and 11). Characters "A" to "I" in Figures 10 and 11 correspond to features discussed in the text.

6.1. Subducting oceanic lithosphere

The first-order feature of the velocity models is the easterly dipping high-v_p (> 8.0 km/s) region associated with the subducting lithosphere ("A" in Figure 10). This high-v_p region is overlaid by a wedge-like region of v_p between 6 and 7 km/s mainly representing the continental forearc ("B"). West of 73° W the prominent, focused and also gently dipping patch of seismicity between 20 and 40 km depth (in the cross sections seen as aligned hypocenters) is also located within the region of $v_p < 7$ km/s (see also Figure 12). Assuming this seismicity patch is situated at the plate interface, the oceanic crust is characterized by v_p around 7 km/s. The exact position of the oceanic Moho and, in turn, the thickness of the oceanic crust cannot be resolved by our tomographic images but the images are in accordance with a 5 to 8 km thick oceanic crust (see also the synthetic test, Figure 8 A). This range is also in agreement with results of a preliminary receiver function study [*Rietbrock et al.*, 2007] and onshore and offshore seismic measurements [*Krawczyk and SPOC Team*, 2003; *Contreras-Reyes et al.*, 2007b].

Down to a depth of 50 km the topmost part of the downgoing lithosphere is characterized by a pronounced, large-scale anomaly of elevated v_p/v_s ratio of about 1.8 which can mainly be attributed to the oceanic crust and uppermost oceanic mantle (see Figures 10, "C", and 12). The values in this part of the model can well be explained by metamorphosed mid-ocean ridge basalt (MORB) or gabbro (blueshist facies) anticipated for large parts of the subducting oceanic crust and partially hydrated mantle [*Hacker et al.*, 2003] under the given temperature and pressure regime in the region. They are in agreement with offshore seismic studies where they had been interpreted as hydrated and altered crustal and upper mantle material due to trench-outer rise bending [e.g., *Contreras-Reyes et al.*, 2007a]. Similar high v_p/v_s ratios in the downgoing slab had also been found in other subduction zones [e.g., *Shelly et al.*, 2006]. Also *Ranero and Sallares* [2006] proposed intense bending-related faulting and related hydration of the material for the Antofagasta region in northern Chile. The lower bound and how deep this anomaly reaches into the mantle are not resolved.

A pronounced, easterly dipping low velocity layer at depths between 50 and 80 km east of 72.5° W most likely reflects the continuation of low velocity material of the subducting oceanic crust ("D") sandwiched between the high-v_p zones (up to 8.2 km/s) of the continental mantle above ("E") and the oceanic mantle below ("A"). Although smeared in the tomographic images this observation clearly confirms the existence of low v_p oceanic crust at this depth previously found elsewhere by the observation of seismic guided waves from intermediate depth earthquakes [e.g., *Abers*, 2000; *Martin et al.*, 2003, 2005].

Seismicity at depths larger than 50 km, although not as focused and rather diffusely distributed, tends to be mainly situated within this low-velocity region. At this depth we also expect the onset of the intermediate seismicity related to dehydration embrittlement [*Kirby et al.*, 1996].

6.2. Marine forearc

The off-shore crustal forearc is characterized by low v_p (< 5km/s) and a very high v_p/v_s of larger than 2 ("F"). These low v_p values most likely reflect fluid-saturated material of the recent and permo-triassic accretionary complex. In particular, the distribution of low v_p correlates well with the extent of the forearc basins which developed at the inner shelf slope (see Figure 2). Although some vertical and horizontal smearing in these regions must be taken into account, the very high v_p/v_s here indicates fluid-saturated sediments which are partially overpressured [e.g., *Behrmann*, 1991; *Eberhart-Phillips et al.*, 2005]. This finding supports observations at the erosive margin of middle America [*Ranero et al.*, 2008]. There, most fluid contained in the sediment pores (of the marine forearc) and liberated by early dehydration reactions drains from the plate boundary through a fractured upper plate rather than migrating along the décollement toward the deformation front as described for accretionary prisms.

The uppermost, often unconsolidated and water saturated marine sediments right beneath the ocean bottom stations might also contribute significantly to the high v_p/v_s ratios for rays traveling within the marine forearc region [*Mallick and Dutta*, 2002]. To test this, we compare $(t_s - t_p)/t_p$ values, which are directly related to average v_p/v_s ratios along the corresponding raypaths, observed at different groups of stations (see Figure 13). In particular, we compare the $(t_s - t_p)/t_p$ values of offshore events (east of 73.3° W) observed at OBS stations to those observed at Mocha island stations which are at a comparable forearc position but are not situated at the sea floor. Most of the raypaths from these offshore events to OBS stations show high to very high average v_p/v_svalues (white symbols in Figure 13). However, raypaths to the two stations on Isla Mocha (dark grey symbols in Figure 13) show similar high average v_p/v_s values of up to 2 which supports the idea that the high values observed at the OBS stations are not just smeared site effects but indeed reflect the deeper marine forearc structure.

We suggest that the high v_p/v_s in this frontal part of the forearc reflects the high content with fluids which are overpressured and may be liberated from the subducting slab and expelled from the subduction channel in this depth range (i.e., < 20 km). It is interesting that this anomaly spatially coincides with the region of the plate interface lacking 'minor' seismicity. Furthermore, the eastern border coincides roughly with the position where a temperature of 100 to 150° C is reached at the plate interface [*Völker et al.*, 2007]. Here, the smectite to illite transition is expected which is assumed to be responsible for variations in mechanical properties and rigidity along the plate interface [*Vrolijk*, 1990]. Alternatively, other pressure- and temperature-dependent processes, such as cementation, consolidation and slip localization with increased shearing may play an important role in changing the frictional properties of subduction zone faults [*Saffer and Marone*, 2003]. Finally, the spatial coincidence of the anomaly and the distribution of seismicity might indicate that the decrease in overpressure with depth leads to increased effective stress across the decollement allowing for seismogenesis as suggested e.g. by *Spinelli et al.* [2006].

6.3. Central forearc crust

The wedge-shape prism of the frontal on-shore forearc ("B") appears as a volume with velocities gradually increasing from 6 km/s at a depth of 10 km to 7 km/s at a depth of 45 km. Velocities above depths of 30 to 40 km are in good agreement with previous refraction seismic studies [*Krawczyk et al.*, 2006]. They can be interpreted as mainly reflecting the metasediments of the permo-triassic accretionary wedge ('Eastern' and 'Western Series') and, in the northern part, the granites of the coastal batholith (see section 2). Sediments of the CD are well imaged by low v_p down to ca. 5 km depth ("G"). No pronounced differences in the shallower (< 20 km depth) velocity structure north and south of the crustal LSZ can be recognized.

The low v_p values smaller than 7 km/s within the crust extend in a wedge like shape down to 50 km at 72.7° W, suggesting an easterly increasing crustal thickness. V_p/v_s within this zone is moderate or slightly lower than average. Isolated anomalies of elevated v_p/v_s are only locally found at midcrustal levels. No subhorizontal layering at the depth of the crust or mantle can be observed.

Furthermore, no v_p typical for lower crustal material can be observed at greater depth and the reduced v_p/v_s in the part directly above the subducting plate clearly discriminates this structure from the underlying subducting crust characterized by high v_p/v_s (see above). Moreover, an easterly dipping low-velocity layer is found in the lower forearc crust ("I"). This layer is situated from 20 km depth beneath the coast to a depth of 40 km beneath the CD and has a thickness of approximately 20 km. We interpret these low velocities as subducted sediments or offscraped forearc material (e.g., of the accretionary wedge) dragged downward by the subduction. A similar low-velocity layer had been found in the Cascadia subduction zone [*Ramachandran et al.*, 2006] where it had been interpreted as due to trapped fluids, highly sheared lower crustal rocks, and/or underthrusting accretionary rock. Also *Brocher et al.* [1994] found a lower crustal low velocity layer in the Alaska subduction zone at a similar position.

This low velocity channel ("I") is best expressed south of 38° S, where the LSZ, the prominent and long-lasting dissection of the South Central Chilean continental forearc is found. While to the north older arc granitoids and continental material form the forearc, the Permo-Triassic metasediments of the paleo wedge ('Western Series') are better preserved south of it [*Aguirre et al.*, 1972] and could be responsible for the pronounced low-velocity layer in this part.

6.4. Mantle wedge

Beneath 30 km depth the wedge shaped crustal forearc is bounded to the east by high v_p exceeding 8 km/s ("E"). This high v_p structure, which reaches shallow levels of 30 km depth beneath the CD and stretches for more than 100 km in N-S direction, is interpreted as continental mantle. Receiver function studies [*Yuan et al.*, 2006] and previous regional tomographic studies [*Bohm*, 2004] confirmed the regional character of this updomed mantle and estimated a crustal thickness of approximately 40 km east of 72.7° W. Surprisingly, a similar, arched forearc mantle structure is found 500 km further south [*Lange*, 2008] supporting the assertion that this feature is a large-scale characteristic of the continental forearc. This arched forearc mantle suggests a crustal thinning beneath the CD possibly related to forearc extension [*Munoz et al.*, 2000; *Bohm*, 2004]. Alternatively, it could be related to the overriding of the subduction zone by the South-American continent as suggested by numerical simulations [*Faccenda et al.*, 2007].

Moderate v_p/v_s ratios of this anomaly indicate this is lithospheric mantle in the western part; the asthenospheric wedge, indicated by elevated v_p/v_s, can be identified east of 72.1° W. The position of the recent magmatic arc as well as the anticipated depth of the subducting slab of about 100 km at this position support this finding. However, this longitude is beyond the well resolved region.

The hydration of the mantle wedge has been discussed for many subduction zones with important consequences for the megathrust and the frictional behavior [e.g., *Graeber and Asch*, 1999; *Bostock et al.*, 2002; *Kamiya and Kobayashi*, 2000; *Peacock and Hyndman*, 1999; *DeShon and Schwartz*, 2004; *Ramachandran et al.*, 2006; *Rossi et al.*, 2006]. Mantle serpentinization would favor stable aseismic sliding thus limiting the downdip extension of the seismogenic zone [see *Hyndman and Peacock*, 2003, and references therein]. Also in our study area, *Krawczyk and SPOC Team* [2003] and *Krawczyk et al.* [2006] had hypothesized a hydrated mantle below 35 km depth mainly based on refraction seismic investigations. For hydrated (i.e. serpentinized) parts of mantle material reduced v_p and elevated v_p/v_s are expected [e.g., *Christensen*, 1966, 1996; *Carlson and Miller*, 2003; *Courtier et al.*, 2004]. We observe very low $v_p < 7km/s$ in this depth range, which would be indicative of a high degree of sepentinization (>35%) if we have continental mantle material in this depth range. However, we do not find the significantly elevated v_p/v_s within this volume as may be expected for the proposed amount of serpentinization [e.g., *Christensen*, 1966, 1996; *Carlson and Miller*, 2003]. Therefore, we interpret these values at this position as lower crust, possibly formed by the long-lasting down-dragging of crustal material to greater depth (see also above).

However, we see indications for rather isolated, smaller anomalies with moderate v_p (7 km/s $< v_p <$ 8 km/s) and v_p/v_s >1.9 which meet the mentioned requirements for serpentinized mantle material ("H"). According to laboratory studies these anomalies could indicate localized pockets of hydrated mantle with less than 20% serpentinization.

A reason for the obviously missing large-scale hydrated mantle wedge in the South Central Chilean Subduction Zone could lie in the compressional regime of the forearc in this particular subduction zone as recently discussed by *Seno* [2005] for Japan. *Seno* [2005] proposes, that in a compressional regime, the water released from the subducting crust escapes updip through the fractured conduit at the plate interface (no mantle serpentinization). If the wedge is tensional, the water released from the subducting crust escapes into the mantle wedge thus yielding serpentinization.

6.5. Characterization of the seismogenic zone

A prominent, focused patch of seismicity collocated in an easterly-dipping plane appears between 20 and 40 km depth beneath the coastal area (see Figure 3). This patch is observed by our network but is also a persisting feature documented in the teleseismic catalogs and here many of the large earthquakes in the last century nucleated (Figure 1). Most earthquakes within this patch are thrust events [*Bruhn*, 2003]. We interpret this patch of seismicity as 'minor' or background seismicity frequently occurring at the contact between oceanic and continental plate in the interseismic cycle. While toward the south the diminishing seismicity would be consistent with a locked section of the thrust, this patch gives evidence for ongoing interseismic deformation at the plate interface (subduction channel) at this specific position [*Cloos and Shreve*, 1988]. According to *Barrientos and Ward* [1990] the largest slip of the 1960 earthquake (larger than 40 m) occurred south of this patch. The location of the patch itself experienced only moderate slip of approximately 5 m (see also Figure 1) indicating that significant stress at the plate interface had not built up. *Haberland et al.* [2006] related these differences in stress concentrations at the plate interface to upper plate structures related to the LSZ.

The v_p structure, hypocenter position and receiver function studies, allowing for a 5 to 8 km thick oceanic crust as shown in Section 6.1, confirm the interpretation that the seismicity patch is situated at the plate interface. Figures 12 shows that the seismicity patch separates a high v_p/v_s region below (oceanic crust and uppermost mantle) from a region with reduced v_p/v_s (overlying forearc crust) which we interpreted as accreted/underplated crustal material (see discussion above). Moreover, the low v_p/v_s anomaly in the latter region suggests that no free fluids are present in this part of the crust. If free fluids indeed do escape from the lower plate (i.e., expelled due to compaction or liberated by phase transformations within the subducting lithosphere at this depth), this suggests the plate interface forms an impermeable seal as, for example, proposed by *Husen and Kissling* [2001] for northern Chile. Our images suggest that this seal might extend at least down to 50 km depth.

It appears that the earthquakes at the plate interface are situated at the edge of, but still within the anomaly of, elevated v_p/v_s rather than outside of it. Overpressured fluids within the subduction channel could be responsible for an increased v_p/v_s contributing to the larger high v_p/v_s anomaly mainly related to the lower plate.

6.6. Implications for mega-thrust earthquake development and rupture extent

As shown above, the v_p images indicate a rather large crustal thickness in the forearc region of up to 50 km. It had been proposed that the width of the seismogenic zone is controlled either by the depth at which the continental Moho intersects with the plate interface or by the depth at which the temperature at the interface is between 350° and 450° C [*Oleskevich et al.*, 1999; *Hyndman et al.*, 1997]. Controlled mainly by the age of the subducting plate (25 to 30 Myrs at the trench today) these temperatures at the interface are reached at a depth of 45 - 60 km in our study area [*Völker et al.*, 2007]. The large crustal thickness shown in our tomographic images suggests a wide contact zone between the crust of the upper plate and the subducting plate. This, in turn, may support the development of a large asperity favoring the accumulation of stress over a long time. Disregarding whether the downdip limit of seismogenic zone in the study area is controlled by the temperature regime or the crustal structure, it seems unlikely to be defined by the 'minor' interplate seismicity, and large and great earthquakes may release strain accumulated along a much wider fault.

Nevertheless, *Simoes et al.* [2004] showed that in the case of the Sumatra subduction zone the locked fault zone extends even below the continental Moho suggesting that either the mantle is not serpentinized or that the presence of serpentine does not necessarily imply stable sliding.

7. Conclusions

With an exceptionally dense, temporary seismological network observing signals from both local earthquakes and artificial shots we were able to image the structure of the continental forearc and the subducting oceanic plate of the South-Central Chilean subduction zone at high resolution. S-wave observations allowed resolution of v_p/v_s anomalies that are closely linked to petrophysical parameters and the processes involved in the formation of the forearc crust and the earthquake generation.

Our main results are (see also summarizing Figure 14):

- High v_p/v_s ratios reflecting MORB and serpentinization of upper (oceanic) mantle material agree well with results from laboratory analysis [*Hacker et al.*, 2003] and offshore seismic studies [*Contreras-Reyes et al.*, 2007b, a]. The alteration of the downgoing lithosphere might be due to offshore, bending-related deep faulting. Subducted oceanic crust is well resolved (by a pronounced low v_p channel) down to a depth of 100 km. The change of v_p/v_s with depth (at approx. 50 km depth) might reflect phase transformations.

- High v_p/v_s and low v_p values in the marine forearc indicate overpressured sediments and expelled water. This anomaly spatially correlates with the frontal region characterized by reduced 'minor' seismicity indicating the aseismic region.

- We infer a large crustal forearc thickness of up to 50 km beneath the coastal cordillera. P velocities in the deeper part are lower than average lower crustal velocities and form a deep crustal low velocity layer. V_p/v_s of this region is rather low. We interpret this as originally upper crustal material or material from the (paleo) accretionary wedge and trench sediments transported to greater depth.

- We have indications for locally hydrated mantle in the continental mantle wedge but not for widespread hydrated mantle.

- Part of the plate interface is clearly defined by a patch of high seismicity beneath the coastal ranges which is the nucleation area of large earthquakes in the area (including the 1960 earthquake) rupturing neighboring large asperities [see also *Hackney et al.*, 2006]. This patch might be related to stress concentrations at the plate interface (via active, crustal transverse faults) [*Haberland et al.*, 2006] at the northern end of a crustal forearc sliver east of the LOFZ [see also *Wang et al.*, 2007] and *Lange et al.* [2006].

- We have an indication for the presence of fluids at the plate interface (subduction channel), however, it seems that this zone is rather an impermeable seal.

- The seismogenic zone seems to be rather wide according to the derived crustal structure and thermal considerations (reaches down to 50 km depth). This value is consistent with previous studies [e.g., *Tichelaar and Ruff*, 1991]. It is conceivable that this wide contact zone supports the formation of very large asperities essential for the development of mega thrust earthquakes.

In order to better understand the general role of forearc structure on the mega-thrust earthquake development and the processes involved we strongly suggest collection of equally high quality data at other parts of the subduction segment and/or at other subduction zones.

Acknowledgments. The TIPTEQ project is financed by the German BMBF and DFG through the R&D-programm GEOTECHNOLOGIEN, grant 03G0594C (publication no. GEOTECH - 223). Thanks to the GIPP (GFZ Potsdam) for providing the instruments. We are indebted to the TIPTEQ controlled seismics group for providing shot locations and origin times. We are grateful to all field groups for their excellent work, to the master and crew of R/V "SONNE" cruise SO 181 for the off-shore deployment, and to J. Bribach, J. Mechie, and G. Hermosilla in particular for station service during the active experiment. We appreciate very much the valuable comments and suggestions by Associate Editor D. Toomey and two anonymous reviewers. All figures were made with the GMT software package [*Wessel and Smith*, 1998]. Thanks also to A. Siebert for help with Figure 14.

References

Abers, G. A., Hydrated subducted crust at 100-250 km depth, *Earth Plan. Sci. Lett.*, *176*, 323–330, 2000.

Aguirre, L., F. Herve, and E. Godoy, Distribution of metamorphic facies in Chile - an outline, *Krystallinikum*, *9*, 7–19, 1972.

Angermann, D., G. Baustert, R. Galas, and S. Y. Zhu, EPOS.P.V3 (Earth Parameter & Orbit System): Software user manual for GPS data processing, *Technical report*, GeoForschungsZentrum, Potsdam, Germany, 1997.

Bangs, N. L., and S. C. Cande, Episodic development of a convergent margin inferred from structures and processes along the southern Chile margin, *Tectonics*, *16*(3), 489–503, 1997.

Barrientos, S., and S. Ward, The 1960 Chile earthquake: inversion for slip distribution from surface deformation, *Geophys. J. Int.*, *103*, 589–598, 1990.

Behrmann, J., Conditions for hydrofracture and the fluid permeability of accretionary wedges, *Earth Planet. Sci. Lett.*, *107*, 550–558, 1991.

Bohm, M., 3-D Lokalbebentomographie der südlichen Anden zwischen 36° und 40° S, Dissertation, Freie Universität Berlin, 2004.

Bostock, M. G., R. D. Hyndman, S. Rodenay, and S. M. Peacock, An inverted continental Moho and serpentinization of the forearc mantle, *Nature*, *417*, 536–538, 2002.

Brocher, T., G. S. Fuis, M. A. Fisher, G. Plafker, M. J. Moses, J. J. Taber, and N. I. Christensen, Mapping the megathrust beneath the northern Gulf of Alaska using wide-angle seismic data, *J. Geophys. Res.*, *99*(B6), 11,663–11,686, 1994.

Bruhn, C., Momententensoren hochfrequenter Ereignisse in Südchile, Dissertation, Universität Potsdam, 2003.

Byrne, D., D. Davis, and L. Sykes, Loci and maximum size of thrust earthquakes and the mechanics of the shallow region of subduction zone, *Tectonics*, *7*(4), 833–857, 1988.

Carlson, R. L., and D. J. Miller, Mantle wedge water contents estimated from seismic velocities in partially serpentinized peridotites, *Geophys. Res. Lett.*, *30*(5), doi:

10.1029/2002GL016600, 2003.

Cembrano, J., F. Hervé, and A. Lavenu, The Liquiñe Ofqui fault zone: A long-lived intra-arc fault system in southern Chile, *Tectonophysics*, *259*, 55–66, 1996.

Christensen, N. I., Elasticity of ultrabasic rocks, *J. Geophys. Res.*, *71*, 5921–5931, 1966.

Christensen, N. I., Poisson's ratio and crustal seismology, *J. Geophys. Res.*, *101*(B2), 3139–3156, 1996.

Cifuentes, I. L., The 1960 Chilean Earthquakes, *J. Geophys. Res.*, *94*(B1), 665–680, 1989.

Cisternas, M., et al., Predecessors of the giant 1960 Chile earthquake, *Nature*, *437*, 404–407, doi:10.1038/nature03943, 2005.

Cloos, M., and R. Shreve, Subduction-channel model of prism accretion, melange formation, sediments subduction, and subduction erosion at convergent plate margins: 1. background and description, *Pure and Applied Geophysics*, *128*(3/4), 455–500, 1988.

Collot, J.-Y., B. Marcaillou, F. Sage, F. Michaud, W. Agudelo, P. Charvis, D. Graindorge, M.-A. Gutscher, and G. Spence, Are rupture zone limits of great subduction earthquakes controlled by upepr plate structures? Evidence from multichannel seismic reflection data across the northern Ecuador-southwest Colombia margin, *J. Geophys. Res.*, *109*, doi:10.1029/2004JB003060, 2004.

Contreras-Reyes, E., I. Grevemeyer, E. R. Flueh, M. Scherwath, and J. Bialas, Effect of trench outer rise bending related faulting on seismic Poisson's ratio and mantle anisotropy: a case study offshore of southern central Chile, *Geophys. J. Int.*, in review, 2007a.

Contreras-Reyes, E., I. Grevemeyer, E. R. Flueh, M. Scherwath, and M. Heesemann, Alteration of the subducting oceanic lithosphere at the southern central Chile trench-outer rise, *Geochem. Geophys. Geosyst.*, *8*, Q07,003, doi:10.1029/2007GC001632, 2007b.

Courtier, A. M., D. J. Hart, and N. I. Christensen, Seismic properties of Leg 195 serpentinites and their geophysical implications, in *Proc. ODP, Sci. Results*, vol. 195 [online], edited by M. Shinohara, M. H. Salisbury, and C. Richter, http://www-odp.tamu.edu/publications/195_SR/104/104.htm, 2004.

DeShon, H., S. Schwartz, A. Newman, V. Gonzalez, J. Protti, L. Dorman, T. Dixon, E. Norabuena, and E. Flueh, Seismogenic zone structure beneath the Nicoya peninsula, Costa Rica, from 3-D local earthquake P- and S-wave tomography, *Geophys. J. Int.*, *164*, 109–124, doi:10.1111/j.1365-246X.2005.02809.x, 2006.

DeShon, H. R., and S. Y. Schwartz, Evidence for serpentinization of the forearc mantle wedge along the Nicoya Peninsula, Costa Rica, *Geophys. Res. Lett.*, *31*, doi:10.1029/2004GL021179s, 2004.

Eberhart-Phillips, D., Three-dimensional structure in northern California coast ranges from inversion of local earthquake arrival times, *Bull. Seismol. Soc. Am.*, *76*(4), 1025–1052, 1986a.

Eberhart-Phillips, D., Three-dimensional structure in northern California coast ranges from inversion of local earthquake arrival times, *Bull. Seismol. Soc. Am.*, *76*, 1025–1052, 1986b.

Eberhart-Phillips, D., and A. J. Michael, Seismotectonics of the Loma Prieta, California, region determined from three-dimensional v_p, v_p/v_s, and seismicity, *J. Geophys. Res.*, *103*(B9), 21,099–21,120, 1998.

Eberhart-Phillips, D., M. Reyners, M. Chadwick, and J.-M. Chiu, Crustal heterogeneity and subduction processes: 3-D vp, vp/vs and Q in the southern North Island, New

Zealand, *Geophys. J. Int.*, *162*, 270–288, doi:10.1111/j.1365-246X.2005.02530.x, 2005.

Eberhart-Phillips, D., D. H. Christensen, T. M. Brocher, R. Hansen, N. A. Ruppert, P. J. Haeussler, and G. A. Abers, Imaging the transition from Aleutian subduction to Yakutat collision in central Alaska, with local earthquakes and active source data, *J. Geophys. Res.*, *111*(B11303), doi:10.1029/2005JB004240, 2006.

Engdahl, E., R. Van Der Hilst, and R. Buland, Global teleseismic earthquake relocation with improved travel time and procedures for depth determination, *Bull. Seismol. Soc. Am.*, *88*(3), 722–743, 1998.

Engdahl, R., and A. Villaseñor, Global seismicity: 1900 - 1999, in *International Handbook of Earthquake and Engineering Seismology*, edited by W. H. K. Lee, H. Kanamori, and P. Jennings, pp. 665–690, IASPEI, part A, Chapter 41, 2002.

Evans, J., D. Eberhart-Phillips, and C. H. Thurber, User's manual for simulps12 for imaging v_p and v_p/v_s: A derivative of the "Thurber" tomographic inversion simul3 for local earthquakes and explosions, *Open File Rep. 94-431*, U.S. Geol. Surv., 1994.

Faccenda, M., T. Gerya, and S. Chakraborty, Styles of post-subduction collisional orogeny: Infuence of conergence velocity, crustal rheology and radiogenic production, *LITHOS*, in press, 2007.

Foulger, G. R., et al., The seismic anomaly beneath Iceland extends down to the mantle transition zone and no deeper, *Geophys. J. Int.*, *142*(3), F1–F5, doi:10.1046/j.1365-246x.2000.00245.x, 2000.

Fuller, C. W., S. D. Willett, and M. T. Brandon, Formation of forearc basins and their influence on subduction zone earthquakes, *Geology*, *34*(2), 65–68, doi: 10.1130/G21828.1;0, 2006.

Glodny, J., et al., Long-term geological evolution and mass-flow balance of the South-Central Andes, in *The Andes - Active Subduction Orogeny, Frontiers in Earth Sciences*, vol. 1, edited by O. Oncken et al., pp. 401–428, Springer, Berlin, Heidelberg, New York, 2006.

Graeber, F., and G. Asch, Three-dimensional models of P wave velocity and P-to S-velocity ratio in the southern central Andes by simultaneous inversion of local earthquake data, *J. Geophys. Res.*, *104*, 20,237–20,256, 1999.

Groß, K., U. Micksch, and TIPTEQ Research Group, The reflection seismic survey of project TIPTEQ - the inventory of the Chilean subduction zone at 38.2°S, *Geophys. J. Int.*, *172*, 565–571, doi:10.1111/j.1365-246X.2007.03680.x, 2008.

Haberland, C., A. Rietbrock, D. Lange, K. Bataille, and S. Hofmann, Interaction between forearc and oceanic plate at the South-Central Chilean margin as seen in local seismic data, *Geophys. Res. Lett.*, *33*, doi:10.1029/2006GL028189, 2006.

Hacker, B. R., S. M. Peacock, G. A. Abers, and S. D. Holloway, Subduction factory 2. Are intermediate-depth earthquakes in subducting slabs linked to metamorphic dehydration reactions?, *J. Geophys. Res.*, *108*(B1), 2030, doi:10.1029/2001JB001129, 2003.

Hackney, R., et al., The segmented overriding plate and coupling at the south-central Chilean margin (36-42° S), in *The Andes - Active Subduction Orogeny*, *Frontiers in Earth Sciences*, vol. 1, edited by O. Oncken et al., pp. 355–374, Springer, Berlin, Heidelberg, 2006.

Husen, S., and E. Kissling, Postseismic fluid flow after the large subduction earthquake of Antofagasta, Chile, *Geology*, *29*(9), 847–850, 2001.

Hyndman, R., and K. Wang, Thermal constraints on the zone of major thrust earthquake failure: The Cascadia subduction zone, *J. Geophys. Res.*, *98*(B2), 2039–2060, 1993.

Hyndman, R., M. Yamano, and D. Oleskevich, The seismogenic zone of subduction thrust faults, *The Island Arc*, *6*, 244–260, 1997.

Hyndman, R. D., and S. M. Peacock, Serpentinization of the forearc mantle, *Earth Planet. Sci. Lett.*, *212*(3-4), 417–432, 2003.

Kamiya, S., and Y. Kobayashi, Seismological evidence for the existence of serpentinized wedge mantle, *Geophys. Res. Lett.*, *27*(6), 819–822, 2000.

Kirby, S., E. R. Engdahl, and R. Denlinger, Intermediate-depth intraslab earthquakes and arc volcanism as physical expressions of crustal and uppermost mantle metamorphism in subducting slabs (overview), in *Subduction: Top to Bottom, Geophys. Monogr. Ser.,* vol. 96, edited by G. E. Bebout, D. W. Scholl, S. H. Kirby, and J. P. Platt, pp. 195–214, AGU, Washington, D.C., 1996.

Kissling, E., W. Ellsworth, D. Eberhart-Phillips, and U. Kradolfer, Initial reference models in local earthquake tomography, *J. Geophys. Res.*, *99*, B10, 1994.

Krawczyk, C., and SPOC Team, Amphibious seismic survey images plate interface at 1960 Chile earthquake, *EOS Trans. AGU*, *84*(32), 301, 304–305, 2003.

Krawczyk, C., et al., Geophysical signatures and active tectonics at the South-Central Chilean margin, in *The Andes - Active Subduction Orogeny*, *Frontiers in Earth Sciences*, vol. 1, edited by O. Oncken et al., pp. 171–192, Springer, Berlin, Heidelberg, New York, 2006.

Lange, C., A. Rietbrock, C. Haberland, K. Bataille, T. Dahm, F. Tilman, and E. Flüh, Seismicity and geometry of the south Chilean subduction zone (41.5° S-

43.5° S): Implications for controlling parameters, *Geophys. Res. Lett.*, *36*, L06,311, doi:10.1029/2006GL029190, 2006.

Lange, C., J. Cembrano, A. Rietbrock, C. Haberland, T. Dahm, and K. Bataille, First seismic record for intra-arc strike-slip tectonics along the Liquine-Ofqui fault zone at the obliquely convergent plate margin of the southern Andes, *Tectonophysics*, *455*(1-4), 14–24, doi:10.1016/j.tecto.2008.04.014, 2008.

Lange, D., The South Chilean subduction zone between 41° S and 43.5° S: Seismicity, structure and state of stress, Ph.D. thesis, Potsdam University, 2008.

Lay, T., and H. Kanamori, An asperity model of large earthquake sequences, in *Earthquake prediction: an international review*, vol. 4, edited by D. Simpson and P. G. Richards, pp. 579–592, AGU, 1981.

Mallick, S., and N. Dutta, Shallow water flow prediction using prestack waveform inversion of conventional 3D seismic data and rock modeling, *The leading edge*, *July*, 675–680, 2002.

Martin, S., A. Rietbrock, and C. Haberland, Guided waves propagating in subducted oceanic crust, *J. Geophys. Res.*, submitted, 2003.

Martin, S., C. Haberland, and A. Rietbrock, Forearc decoupling of guided waves in the Chile-Peru subduction zone, *Geophys. Res. Lett.*, *32*, L23,309, doi: 10.1029/2005GL024183, 2005.

McCaffrey, R., On the role of the upper plate in great subduction zone earthquakes, *J. Geophys. Res.*, *81*(B7), 11,953–11,966, 1993.

Melnick, D., and H. P. Echtler, Morphotectonic and geologic digital map compilations of the south-central Andes (36°-42° S), in *The Andes - Active Subduction Orogeny*, *Frontiers in Earth Sciences*, vol. 1, edited by O. Oncken et al., pp. 565–568, Springer, Berlin, Heidelberg, New York, 2006a.

Melnick, D., and H. P. Echtler, Inversion of forearc basins in south-central Chile caused by rapid glacial age trench fill, *Geology*, *34*(9), 709–712, 2006b.

Melnick, D., B. Bookhagen, H. Echtler, and M. Strecker, Coastal deformation and great subduction earthquakes, Isla Santa María, Chile (37° S), *Geol. Soc. Am. Bull.*, *118*(11), 1463–1480, doi:10.1130/B25865.1, 2006.

Montagner, J.-P., and B. L. N. Kennett, How to reconcile body-wave and normal-mode reference earth models, *Geophys. J. Int.*, *125*, 229–248, 1996.

Mordojovich, C., Sedimentary basins of Chilean Pacific offshore, in *Energy resources of the Pacific region*, *AAPG Stud. Geol*, vol. 12, edited by M. T. Halbouty, pp. 63–82, 1981.

Munoz, J. O., R. Troncoso, P. Duhart, P. Crignola, L. Farmer, and C. Stern, The relation of the mid-Tertiary coastal magmatic belt in south-central Chile to late Oligocene increase in plate convergence rate, *Revista Geologica de Chile*, *27*, 147–167, 2000.

Newman, A., S. Schwartz, V. Gonzalez, H. DeShon, J. Protti, and L. Dorman, Along-strike variability in the seismogenic zone below Nocoya Peninsula, Costa Rica, *Geophys. Res. Lett.*, *29*(20), doi:10.1029/2002GL015409, 2002.

Oleskevich, D., R. Hyndman, and K. Wang, The updip and downdip limits to great subduction earthquakes: Thermal and structural models of Cascadia, south Alaska, SW Japan, and Chile, *J. Geophys. Res.*, *104*(B7), 14,965–14,991, 1999.

Peacock, S. M., and R. D. Hyndman, Hydrous minerals in the mantle wedge and the maximum depth of subduction thrust earthquakes, *Geophys. Res. Lett.*, *26*(16), 2517–

2520, 1999.

Plafker, G., and J. C. Savage, Mechanism of the Chilean earthquake of May 21 and 22, 1960, *Geol. Soc. Am. Bull.*, *81*, 1001–1030, 1970.

Podvin, P., and L. Lecomte, Finite difference computation of traveltimes in very contrasted velocity models. A massively parallel approach and its associated tools, *Geophys. J. Int.*, *105*, 271–284, 1991.

Raitt, R., Seismic-refraction studies of the pacific ocean basin, *Bull. Seismol. Soc. Am.*, *67*, 1623–1640, 1956.

Raitt, R. W., G. G. Shor, T. J. G. Francis, and G. B. Morris, Anisotropy of the Pacific upper mantle, *J. Geophys. Res.*, *74*, 3.095–3.109, 1969.

Ramachandran, K., R. Hyndman, and T. Brocher, Regional P wave velocity structure of the Northern Cascadia subduction zone, *J. Geophys. Res.*, *111*, doi: 10.1029/2005JB004108, 2006.

Ranero, C., and V. Sallares, Geophysical evidence for hydration of the crust and mantle of the nacra plate during bending at the north Chile trench, *Geology*, *32*(7), doi: 10.1130/G20379.1, 2006.

Ranero, C. R., et al., Hydrogeological system of erosional convergent margins and its influence on tectonics and interplate seismogenesis, *Geochem. Geophys. Geosyst.*, *9*, Q03S04, doi:10.1029/2007GC001679, 2008.

Reyners, M., D. Eberhart-Phillips, G. Stuart, and Y. Nishimura, Imaging subduction from the trench to 300 km depth beneath the central North Island, New Zealand, with Vp and Vp/Vs, *Geophys. J. Int.*, *165*(2), 565–583, doi:10.1111/j.1365-246X.2006.02897.x, 2006.

Rietbrock, A., and F. Scherbaum, The GIANT analysis system (graphical interactive aftershock network toolbox), *Seismological Research Letters*, *69*(1), 40–45, 1998.

Rietbrock, A., C. Haberland, K. Bataille, T. Dahm, and O. Oncken, Studying the seismogenic coupling zone with a passive seismic array, *EOS*, *86*(32), 2005.

Rietbrock, A., C. Haberland, D. Lange, T. Dahm, A. Lodge, K. Bataille, F. Tilmann, E. Flueh, and TIPTEQ Research Group, Studying the seismogenic coupling zone with a passive seismic array: The TIPTEQ experiment in Southern Chile, *Geophysical Research Abstracts*, *9*, 06,466, 2007.

Rossi, G., G. A. Abers, S. Rondenay, and D. H. Christensen, Unusual mantle Poisson's ratio, subduction, and crustal structure in central Alaska, *J. Geophys. Res.*, *111*, doi: 10.1029/2005JB003956, 2006.

Saffer, D. M., and C. Marone, Comparison of Smectite- and Illite-rich gouge frictional properties: Application to the updip limit of the seismogenic zone along subduction megathrusts, *Earth Planet. Sci. Lett.*, *215*(1-2), 219–235, 2003.

Seno, T., Variation of downdip limit of the seismogenic zone near the Japanese islands: implications for the serpentinization mechanism of the forearc mantle wedge, *Earth Planet. Sci. Lett.*, *231*(3-4), 249–262, 2005.

Shelly, D. R., G. C. Beroza, H. Zhang, C. H. Thurber, and S. Ide, High-resolution subduction zone seismicity and velocity structure beneath Ibaraki Prefecture, Japan, *J. Geophys. Res.*, *111*(B06311), doi:10.1029/2005JB004081, 2006.

Simoes, M., J. P. Avouac, R. Cattin, and P. Henry, The Sumatra subduction zone: A case for a locked fault zone extending into the mantle, *J. Geophys. Res.*, *109*, B10,402, doi:10.1029/2003JB002958, 2004.

Song, T.-R. A., and M. Simons, Large trench-parallel gravity variations predict seismogenic behaviour in subduction zones, *Science*, *301*, 630–633, 2003.

Spinelli, G. A., D. M. Saffer, and M. B. Underwood, Hydrogeologic responses to three-dimensional temperature variability, Costa Rica subduction margin, *J. Geophys. Res.*, *111*, B04,403, doi:10.1029/2004JB003436, 2006.

Tebbens, S. F., and S. C. Cande, Southeast Pacific tectonic evolution from early Oligocene to present, *J. Geophys. Res.*, *102*(6), 12,061–12,084, 1997.

Thurber, C., Earthquake locations and three-dimensional crustal structure in the Coyote Lake area, central California, *J. Geophys. Res.*, *88*, 8226–8236, 1983.

Thurber, C., Local earthquake tomography: Velocities and v_p/v_s-theory, in *Seismic Tomography: Theory and Practice*, edited by H. Iyer and K. Hirahara, pp. 563–583, Chapman and Hall, New York, 1993.

Thurber, C., and D. Eberhart-Phillips, Local earthquake tomography with flexible gridding, *Comput. & Geosci.*, *25*, 809–818, 1999.

Tichelaar, B. W., and L. J. Ruff, Seismic coupling along the Chilean subduction zone, *J. Geophys. Res.*, *96*(B7), 1991.

Toomey, D., and G. Foulger, Tomographic inversion of local earthquake data from the Hengill-Grensdalur central volcano complex, Iceland, *J. Geophys. Res.*, *94*, 17,497–17,510, 1989.

Tryggvason, A., and B. Bergman, A traveltime reciprocity discrepancy in the Podvin & Lecomte *time3d* finite difference algorithm, *Geophys. J. Int.*, *165*, 432–435, doi:10.1111/j.1365-246X.2006.02925.x, 2006.

Um, J., and C. H. Thurber, A fast algorithm for two-point ray tracing, *Bull. Seismol. Soc. Am.*, *77*, 972–986, 1987.

Uyeda, S., and H. Kanamori, Back-arc opening and the mode of subduction, *J. Geophys. Res.*, *84*, 1049–1061, 1979.

Völker, D., I. Grevemeyer, J. He, K. Wang, and M. Heesemann, Thermal regime of the Chilean subduction zone at 38° S and 43° S - model results and implications for seismicity, in *General Assembly of the European Geosciences Union, Vienna*, pp. EGU2007–A–06,274, 2007.

Vrolijk, P., On the mechanical role of smectite in subduction zones, *Geology*, *18*(8), 703–707, 1990.

Wang, K., Y. Hu, M. Bevis, E. Kendrick, R. S. Jr., R. B. Vargas, and E. Lauria, Crustal motion in the zone of the 1960 Chile earthquake: Detangling earthquake-cycle deformation and forearc-sliver translation, *Geochemistry, Geophysics, Geosystem*, *8*(10), doi:10.1029/2007GC001721, 2007.

Wessel, P., and W. Smith, New, improved version of the Generic Mapping Tools released, *Eos Trans. AGU*, *79*, 579, 1998.

Yuan, X., G. Asch, K. Bataille, G. Bock, M. Bohm, H. Echtler, R. Kind, O. Oncken, and I. Wölbern, Deep seismic images of the southern andes, in *Evolution of an Andean margin: A tectonic and magmatic view from the Andes to the Neuquen Basin (36-39° S)*, vol. SPECIAL PAPER 407, edited by S. Kay and V. Ramos, pp. 61–72, doi: 10.1130/2006.2407(03), 2006.

Phase	Time Span	Total # Stations[a]	Land Equip.	Sea Equip.[b]	Quakes + shots
1	Nov. 2004 – Jan. 2005	65	24 PDAS 41 REFTEK	–	101 94
2	Feb. 2005 – Jun. 2005	120 + 10	120 EDL	4 (2)OBS 6 (4) OBH	309
3	Jul. 2005 – Oct. 2005	20 + 10	20 EDL	4 (2)OBS 6 (4) OBH	29

[a] Land + Sea

[b] Stations producing usable data in brackets

Table 1. TIPTEQ temporary seismic network deployments between November 2004 and October 2005. Last column gives number of earthquakes and shots recorded in respective phase which were used in tomographic inversion.

Model	hor.spac.(km)	vert.spac.(km)	# events[a]	P data var. (s^2)	%	S data var. (s^2)	%
initial 1-D	-	10	274 + 94	0.095	100	0.207	100
coarse 2-D	15	10	274 + 94	0.0613	33	0.200	53
fine 2-D	15	5	274 + 94	0.031	33	0.085	53
3-D	15/20[b]	5	439 + 94	0.018	19	0.061	30

[a] earthquakes + shots

[b] WE/NS

Table 2. Inversion parameter and resulting data variances of our staggered inversion scheme.

Figure 1. Geotectonic situation at the South-Central Chilean margin. The study area (black-outlined box) is located at the northern end of the rupture area of the 1960 Chile earthquake. Hypocentre depicted by black star [*Engdahl and Villaseñor*, 2002]. Black contours (numbers are in m) indicate the slip distribution of the 1960 Chile earthquakes following *Barrientos and Ward* [1990] (isolated patches of slip at depth greater than 100 km are left out for clarity). Small circles depict hypocentre of local earthquakes since 1960 [*Engdahl et al.*, 1998]. Recent volcanoes are indicated by triangles. The intra-arc dextral Liquine-Ofqui shear zone (black line) forms the eastern border of a crustal forearc sliver [*Cembrano et al.*, 1996; *Wang et al.*, 2007]. AP is Arauco Peninsula.

Figure 2. Morphotectonic and lithological units forming the South-Central Chilean forearc after *Melnick and Echtler* [2006a]. Lines indicate crustal faults, dashed lines indicate inferred faults. IM: Isla Mocha; ISM: Isla Santa Maria; AP: Arauco Peninsula; LSZ: Lanalhue shear zone; LOFZ: Liquine-Ofqui shear zone.

Figure 3. Station distribution of the temporary TIPTEQ seismic array. White triangles indicate land stations, gray triangles indicate ocean bottom seismometer stations and gray inverted triangles ocean bottom hydrophone stations. Stations referred to in the text are labeled. See Figure 1 for large scale location of network.

Figure 4. Station (gray inverted triangles) and earthquake (white circles) distribution, and ray coverage (gray lines) at the South-central Chilean margin. Crosses depict the nodes of the tomographic model, white triangles indicate shot locations (along 38°15' S), and star indicates epicenter of the 1960 earthquake [*Engdahl and Villaseñor*, 2002].

Figure 5. Data example. Recordings of a local earthquake (2005-06-16, 01:54:58.54 UTC, 73.982170° W, 37.896500° S, 17 km depth) recorded by land station B504 and OBS station 254. Shown are (from top to bottom) vertical component, North-South component and west-east component (land station) or vertical seismometer component, first and second horizontal component and hydrophone channel (OBS station). P and S picks, respectively, are indicated by gray vertical lines. OBS data is 1 to 20 Hz bandpass filtered.

Figure 6. 1-D v_p model which served as starting model for the 2-D tomographic inversion (white circle and black line, respectively). Above 100 km depth we adopted the 1-D, staircase-like velocity depth function from our VELEST inversion [*Haberland et al.*, 2006, gray line], for greater depth (with lower resolution of the model based on local earthquake observations) we resort to the global average values [e.g., *Montagner and Kennett*, 1996]

Figure 7. Resolution estimate based on analysis of the model resolution matrix along five WE-sections (v_p nodes left, v_p/v_s nodes right). Spread values are shown with different gray values, diagonal element with circles of different size, and the 70% contour line of the resolution kernel (indicating the smearing) are shown by black lines. Only contours of nodes with significant diagonal elements are show and only the contours of every second row are shown for clarity. See text for further information.

Figure 8. Synthetic 2-D models (left) and corresponding inversion results (right) for the synthetic restoration test; black dots indicate local earthquakes of this study. A) V_p model used in all synthetic tests. B) Synthetic v_p/v_s model with a positive anomaly resembling values expected for altered and hydrated oceanic crust and mantle. C) Same as B) but without depth limit and with opposite perturbation. D) V_p/v_s model with anomalies in marine forearc, beneath the CD, and in the mantle wedge. See text for discussion.

Figure 9. 2-D velocity model (v_p top, v_p/v_s bottom). Velocities and v_p/v_s ratios, respectively, are color coded, regions with less resolution (based on analysis of the model resolution matrix and synthetic tests) are shown faded, unresolved regions are blank. Hypocenters of all earthquakes used in the inversion are depicted by white circles and grid nodes are indicated by crosses. The star indicates hypocenter of the 1960 earthquake

Figure 10. Velocity model along five W-E sections through the final 3-D model (v_p left, v_p/v_s right). Velocities and v_p/v_s ratios, respectively, are color coded, regions with lower resolution (based on analysis of the MRM and synthetic tests) are shown faded, unresolved regions are blank. Earthquakes within a 0.5° wide corridor around the particular section are depicted by white circles. Characters "A" to "H" refer to features discussed in text. Star indicates hypocenter of the 1960 earthquake [*Engdahl and Villaseñor*, 2002]

Figure 11. Velocity model along six depth sections through the final 3-D model (v_p). Lines indicate faults according to [*Melnick and Echtler*, 2006a]. See caption of figure 10 for more details.

Figure 12. Closeup of the v_p and v_p/v_s model along 38° S. Circles depict local earthquakes and gray lines illustrate inferred oceanic crust (top of slab and oceanic Moho, interpretation).

Figure 13. S-P travel times (normalized to the P-wave travel time) observed at two coastal onshore stations A403 and C403 (light gray circles and light gray triangle, respectively), the Mocha island stations M501 and SMG1 (dark gray diamond and dark gray triangles), and two OBS stations 253 and 254 (white circles and white squares). Symbols on top indicate longitude of respective stations (see also Figure 3). Steady $(t_s - t_p)/t_p$ values for the onshore stations around 0.75 for a broad range of earthquakes source longitudes indicate an average v_p/v_s for these rays of around 1.75. OBS stations observe very high values for offshore earthquakes (indicating a high v_p/v_s in the offshore forearc) while they observe average values for easterly located earthquakes. The Mocha island stations also see similarly elevated values, although the extreme values are not reached. This indicates that the high values observed at the OBS stations are not just site effects and that lateral (North-South) variations exist.

Figure 14. Interpretative section along approximately 38° S summarizing the main results. Hatched areas indicate enhanced v_p/v_s ratio; white circles indicate hypocenters of earthquakes used in this study; thick black line indicates seismogenic zone. See text for more information.

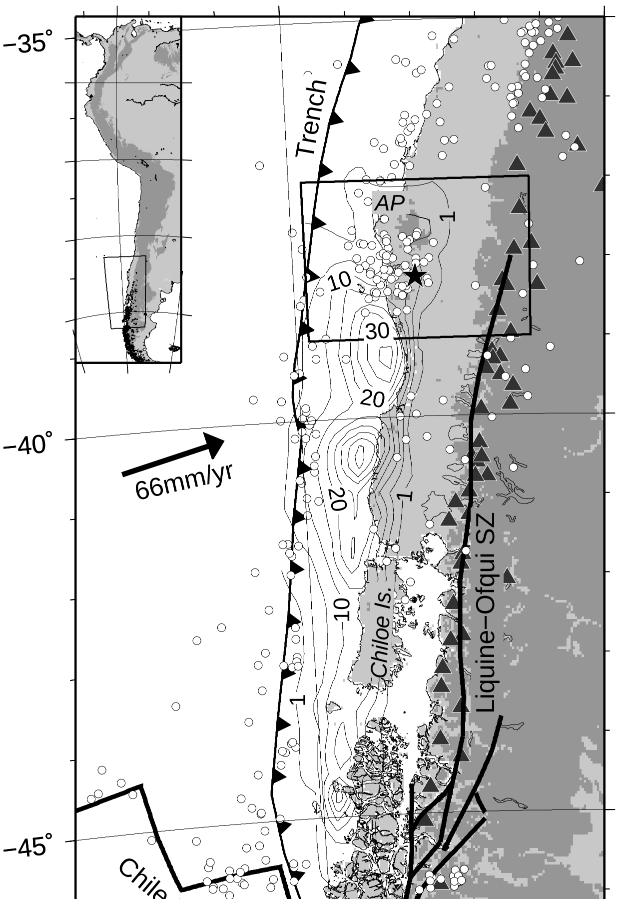

−35°
−40°
−45°
−80°
−75°
−70°
Trench
AP
10
30
20
1
20
10
1
Chiloe Is.
Liquine−Ofqui SZ
66mm/yr
Chile Ridge

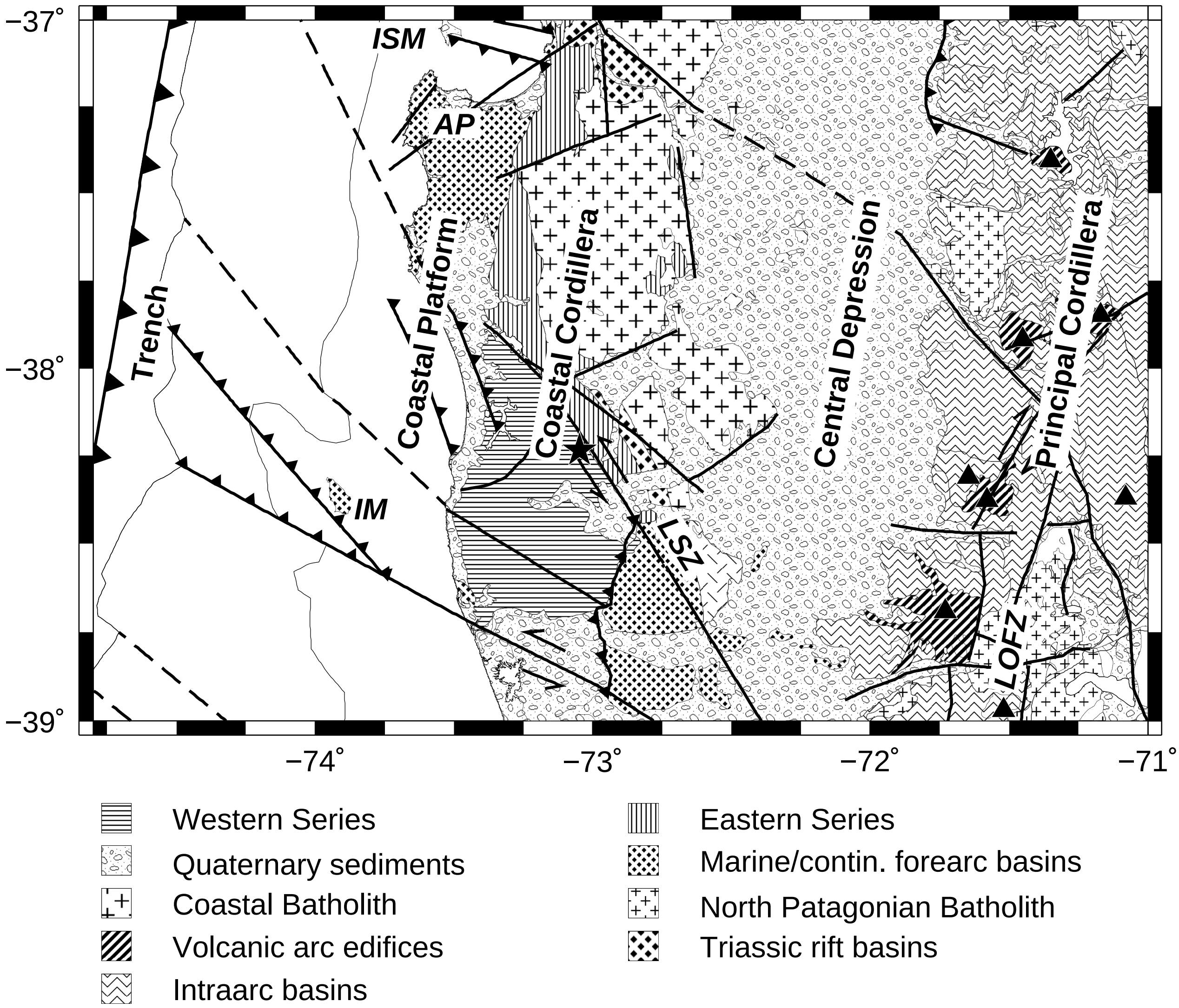

−37°
−38°
−39°
−74°
−73°
−72°
−71°
ISM
AP
IM
Trench
Coastal Platform
Coastal Cordillera
Central Depression
Principal Cordillera
LSZ
LOFZ
Western Series
Quaternary sediments
Coastal Batholith
Volcanic arc edifices
Intraarc basins
Eastern Series
Marine/contin. forearc basins
North Patagonian Batholith
Triassic rift basins

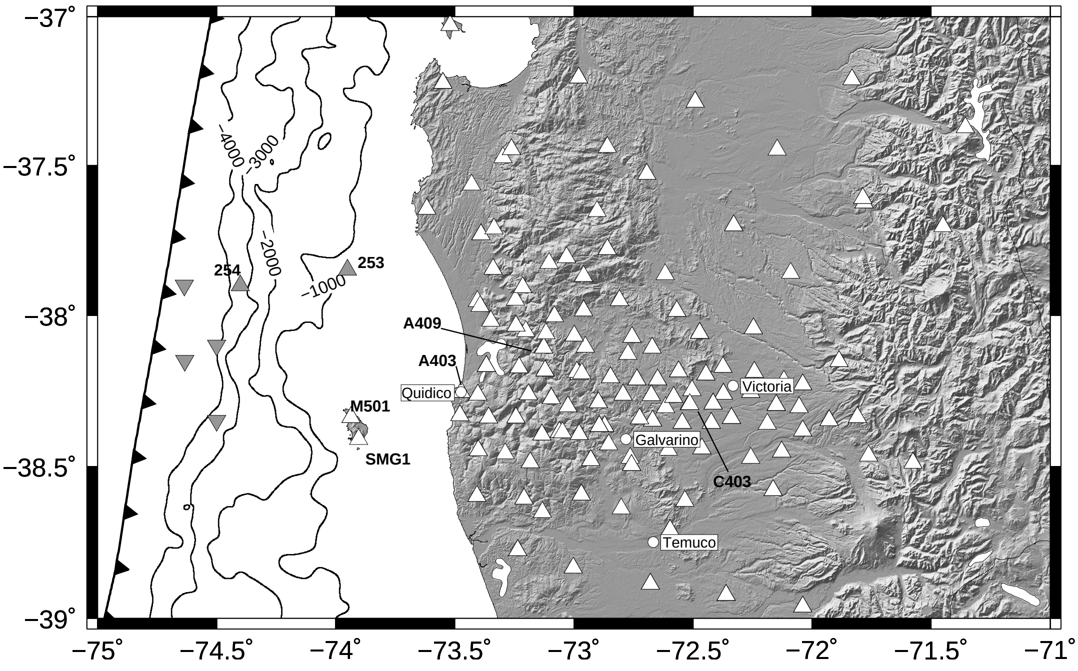
-37°
-37.5°
-38°
-38.5°
-39°
-75°
-74.5°
-74°
-73.5°
-73°
-72.5°
-72°
-71.5°
-71°
-4000
-3000
-2000
-1000
254
253
A409
A403
Quidico
M501
SMG1
Victoria
Galvarino
C403
Temuco

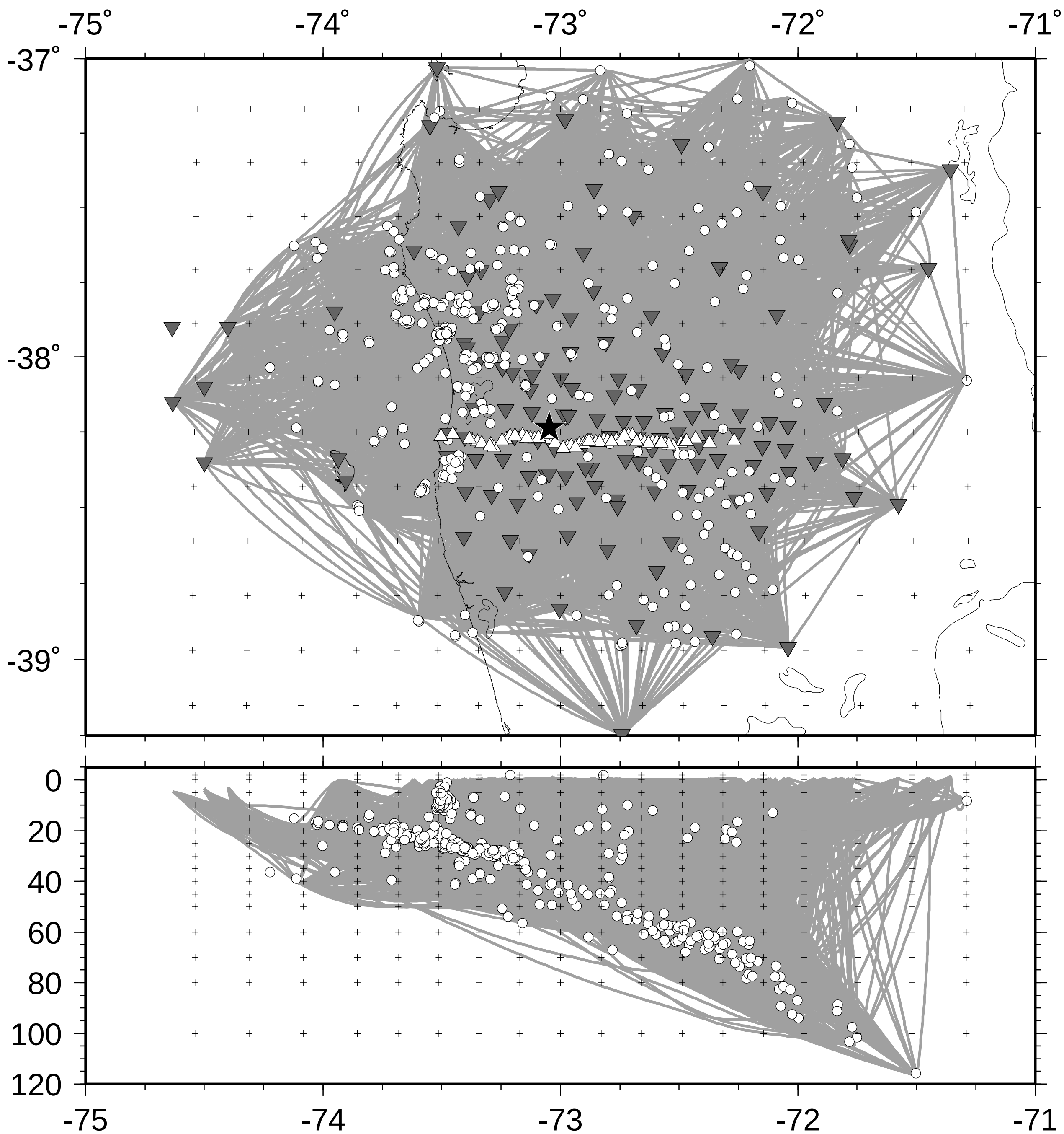

-75°
-74°
-73°
-72°
-71°
-37°
-38°
-39°
0
20
40
60
80
100
120
-75
-74
-73
-72
-71

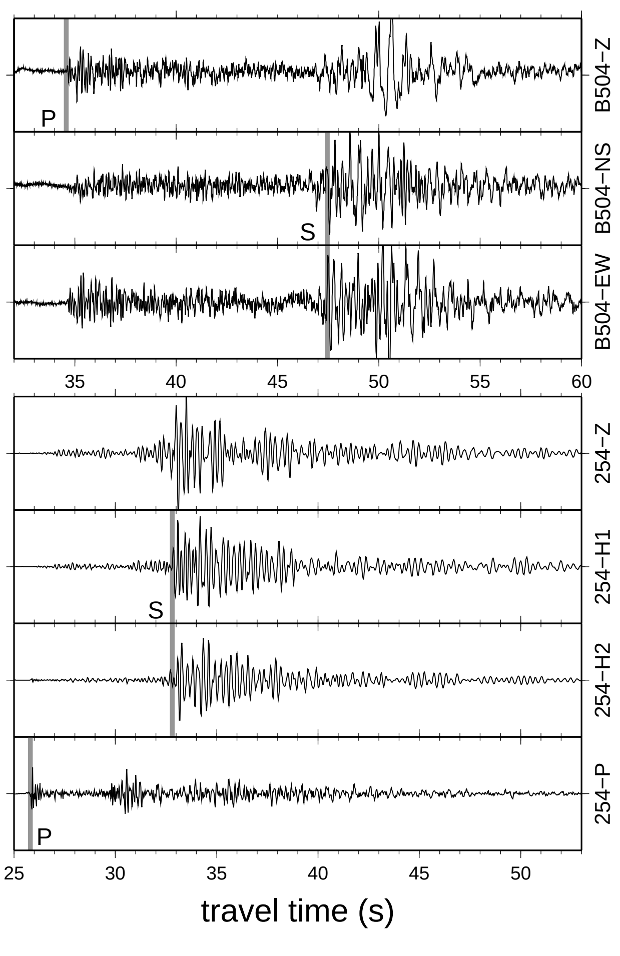
B504−Z
B504−NS
B504−EW
P
S
35
40
45
50
55
60
254−Z
254−H1
254−H2
254−P
S
P
25
30
35
40
45
50
travel time (s)

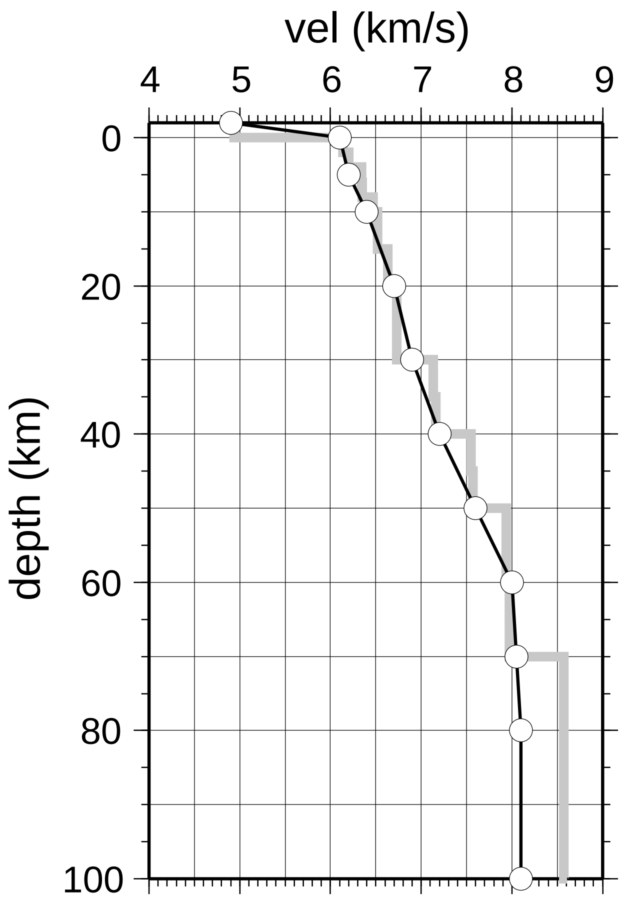
vel (km/s)
4
5
6
7
8
9
depth (km)
0
20
40
60
80
100

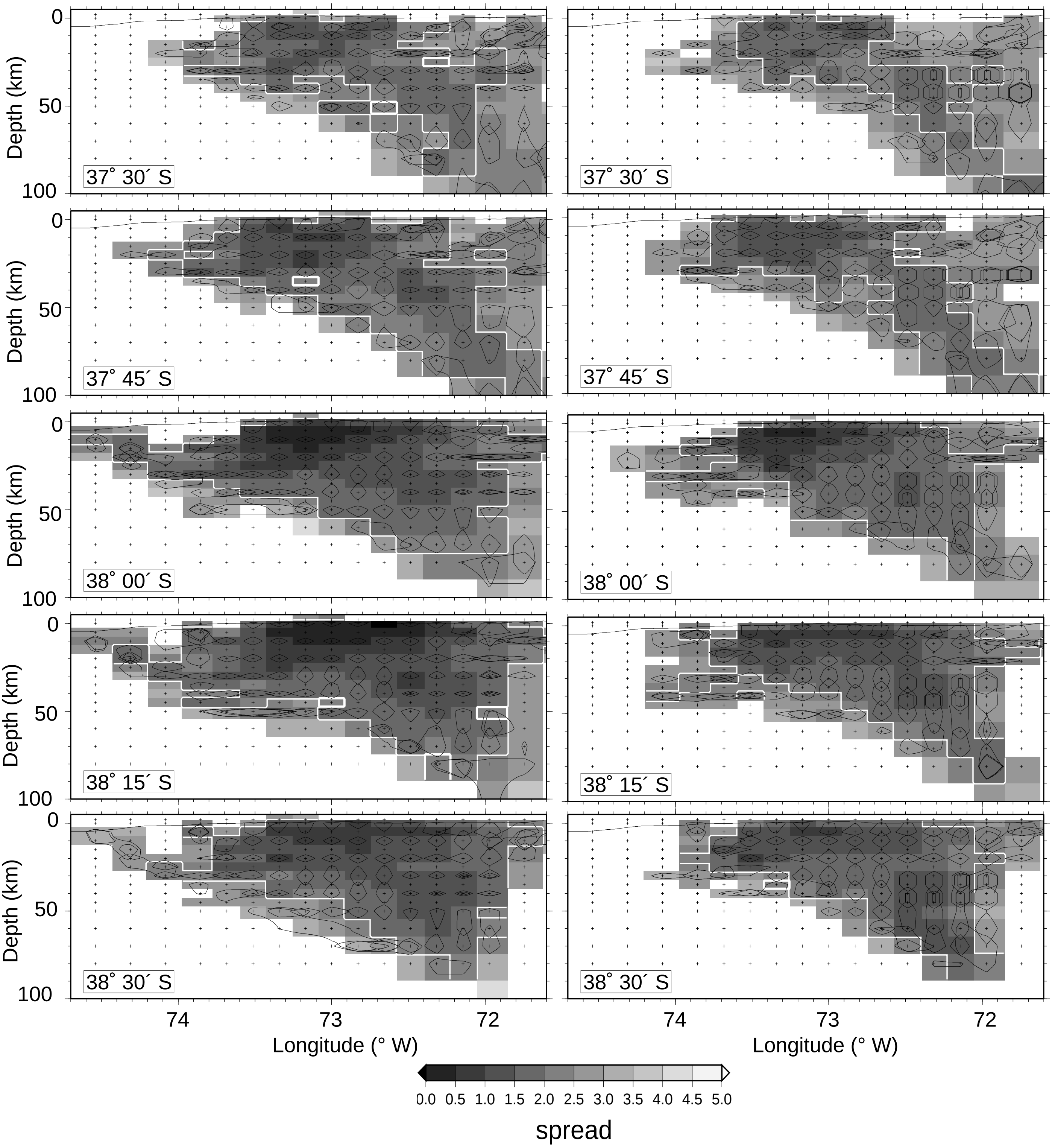

Depth (km)
0
50
100
37° 30´ S
37° 45´ S
38° 00´ S
38° 15´ S
38° 30´ S
74
73
72
Longitude (° W)
0.0 0.5 1.0 1.5 2.0 2.5 3.0 3.5 4.0 4.5 5.0
spread

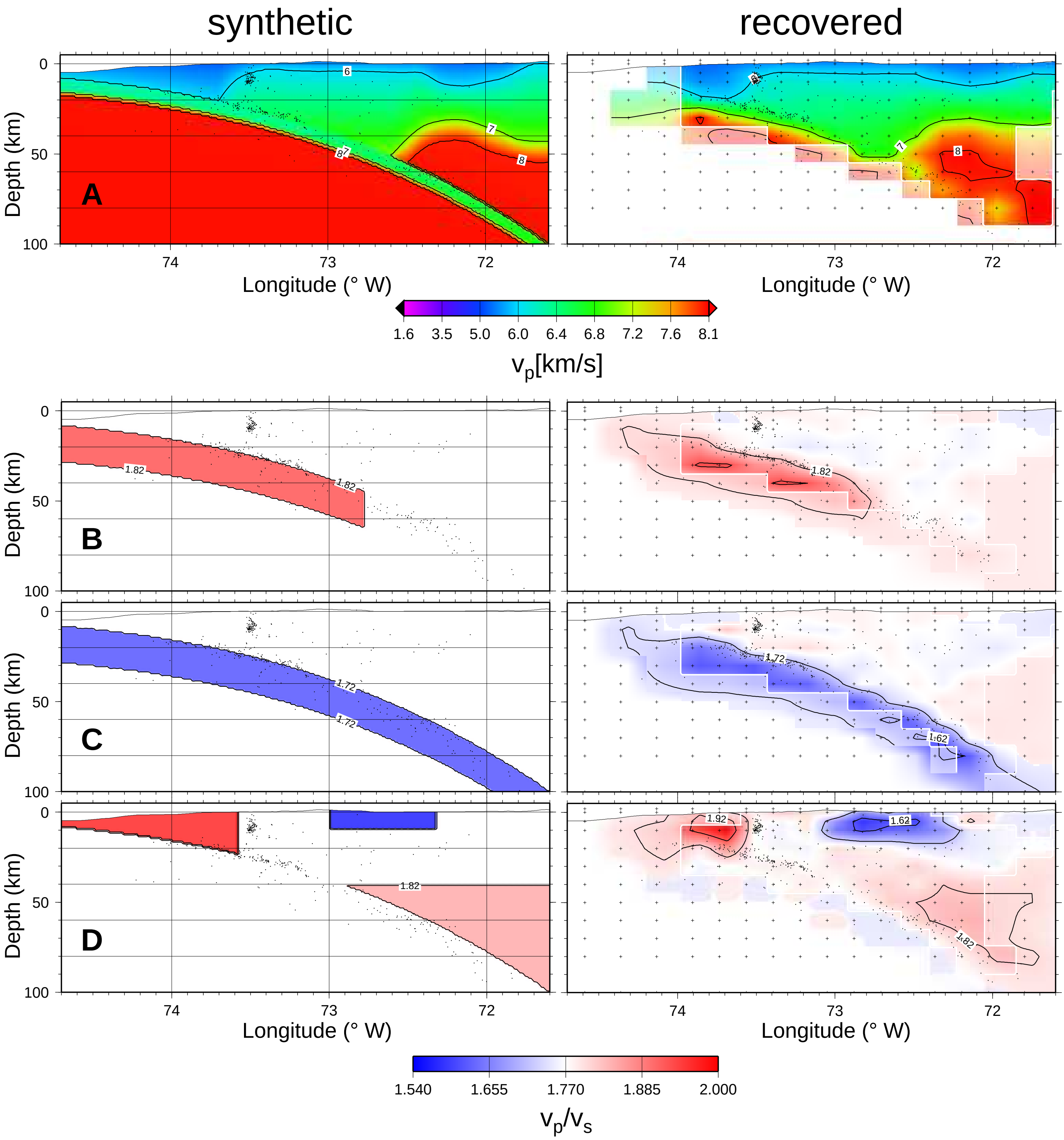

synthetic
recovered
Depth (km)
0
50
100
A
B
C
D
74
73
72
Longitude (° W)
6
7
8
1.82
1.72
1.62
1.92
1.6
3.5
5.0
6.0
6.4
6.8
7.2
7.6
8.1
vp[km/s]
1.540
1.655
1.770
1.885
2.000
vp/vs

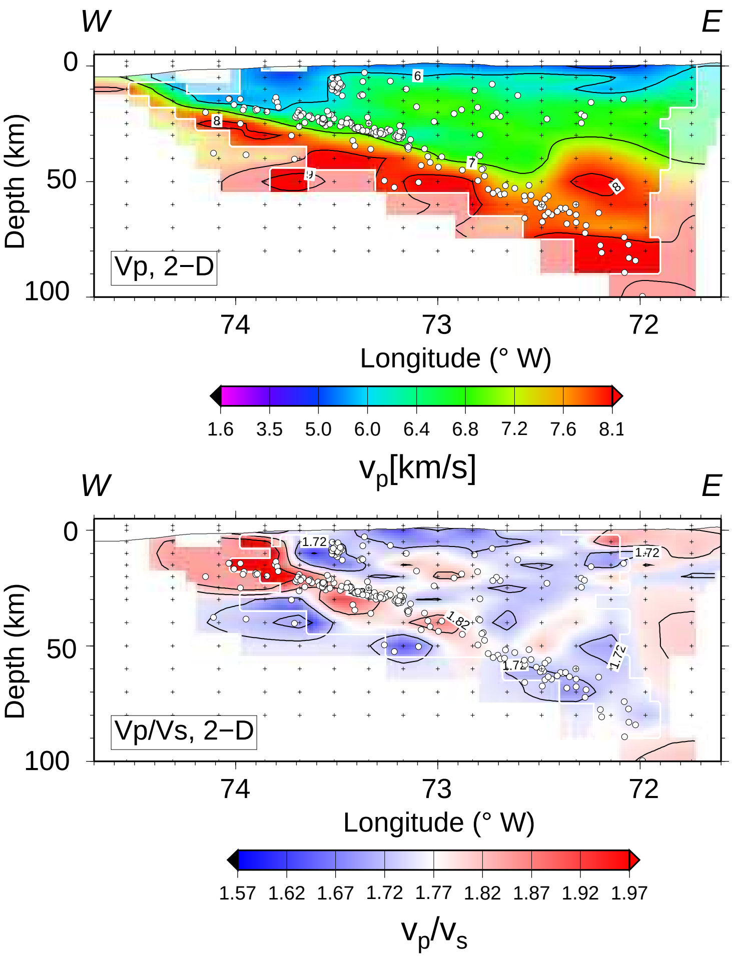

W
E
Depth (km)
0
50
100
Vp, 2−D
74
73
72
Longitude (° W)
1.6
3.5
5.0
6.0
6.4
6.8
7.2
7.6
8.1
vp[km/s]
W
E
Depth (km)
Vp/Vs, 2−D
Longitude (° W)
1.57
1.62
1.67
1.72
1.77
1.82
1.87
1.92
1.97
vp/vs

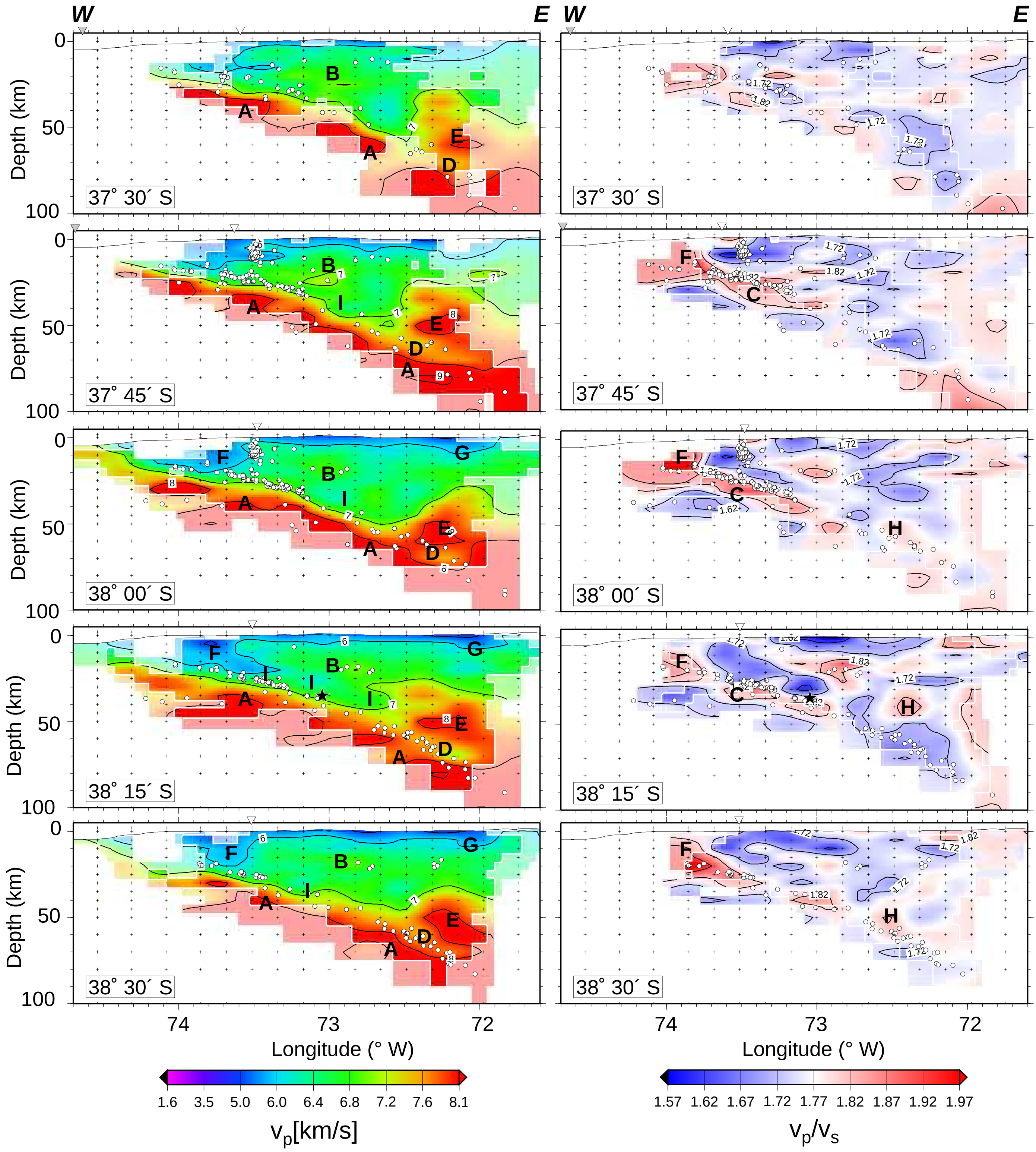
W
E
W
E
Depth (km)
0
50
100
37° 30´ S
37° 45´ S
38° 00´ S
38° 15´ S
38° 30´ S
A
B
C
D
E
F
G
H
I
74
73
72
Longitude (° W)
1.6
3.5
5.0
6.0
6.4
6.8
7.2
7.6
8.1
vp[km/s]
1.57
1.62
1.67
1.72
1.77
1.82
1.87
1.92
1.97
vp/vs

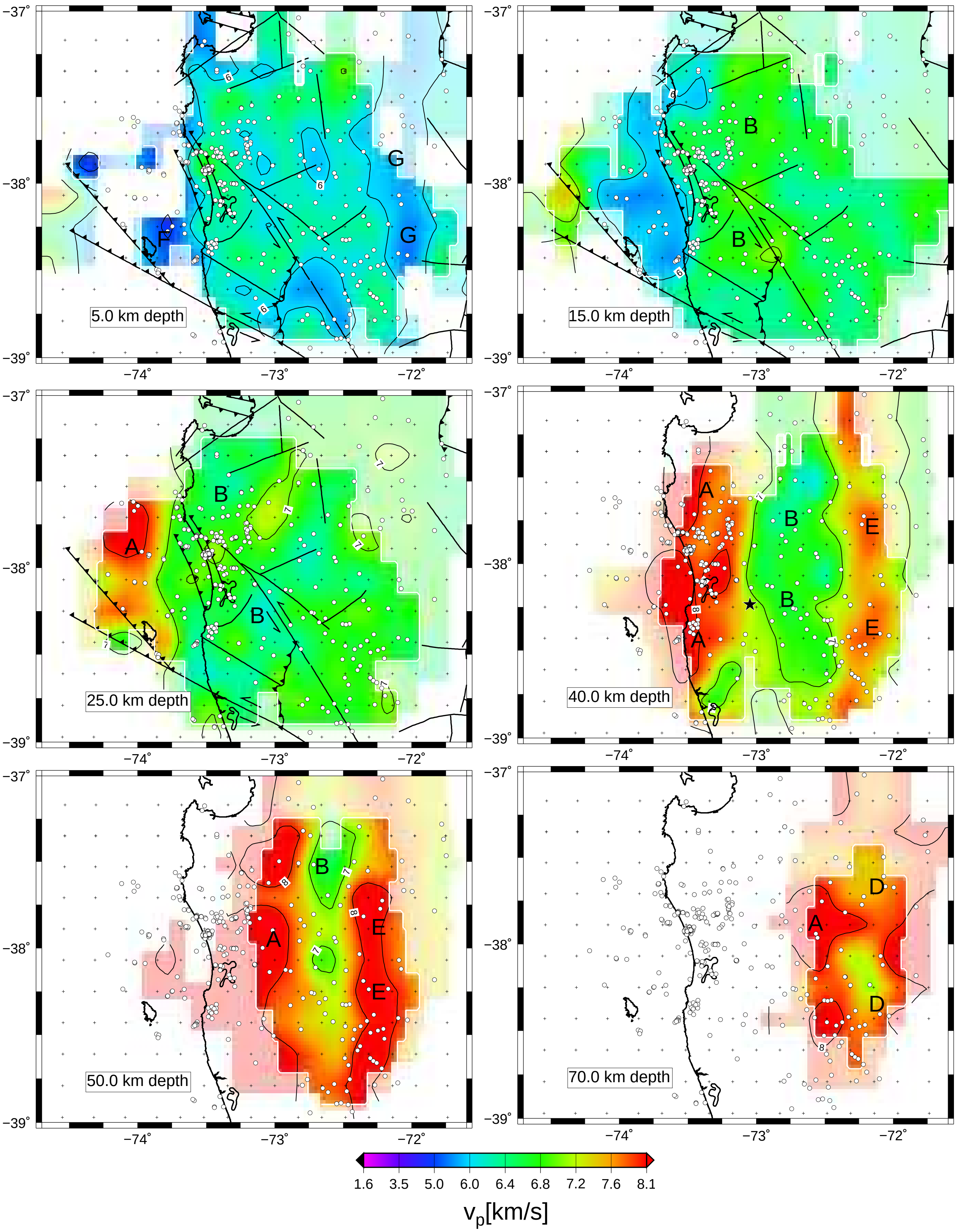

−37°
−38°
−39°
−74°
−73°
−72°
5.0 km depth
15.0 km depth
25.0 km depth
40.0 km depth
50.0 km depth
70.0 km depth
A
B
D
E
F
G
1.6
3.5
5.0
6.0
6.4
6.8
7.2
7.6
8.1
v_p[km/s]

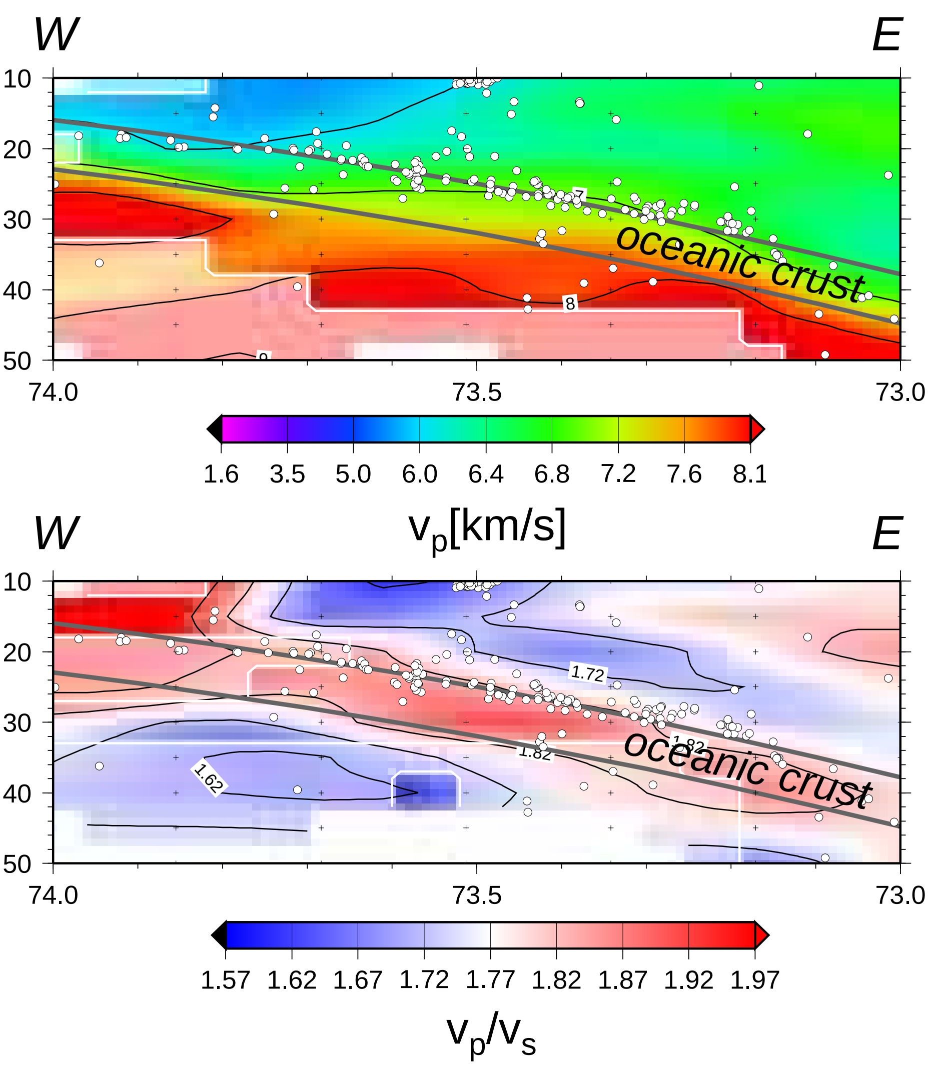
W
E
10
20
30
40
50
74.0
73.5
73.0
oceanic crust
7
8
9
1.6
3.5
5.0
6.0
6.4
6.8
7.2
7.6
8.1
vp[km/s]
W
E
1.72
1.82
1.62
oceanic crust
1.57
1.62
1.67
1.72
1.77
1.82
1.87
1.92
1.97
vp/vs

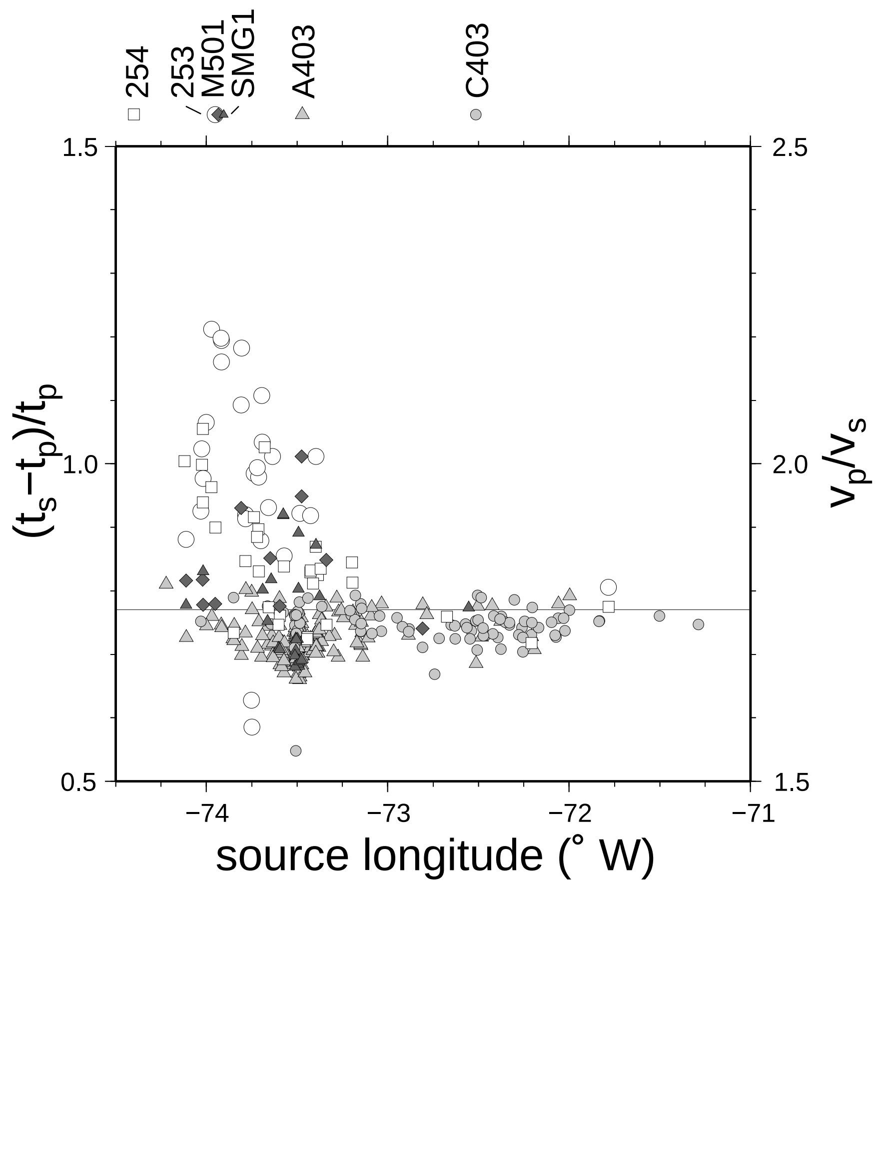
254
253
M501
SMG1
A403
C403
1.5
1.0
0.5
2.5
2.0
1.5
(t_s−t_p)/t_p
v_p/v_s
−74
−73
−72
−71
source longitude (° W)

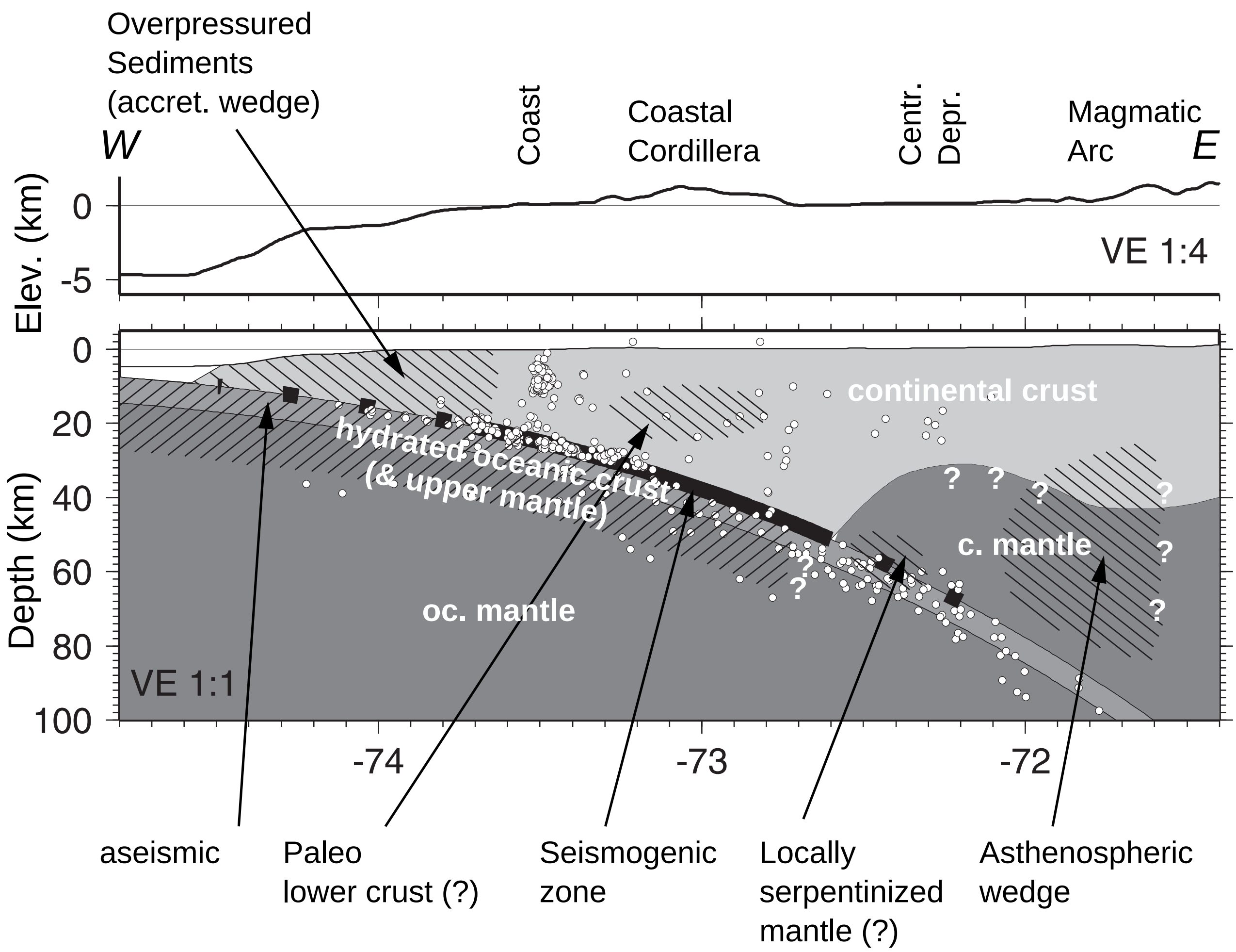

Overpressured
Sediments
(accret. wedge)
W
Coast
Coastal
Cordillera
Centr.
Depr.
Magmatic
Arc
E
Elev. (km)
0
-5
VE 1:4
0
20
40
60
80
100
Depth (km)
continental crust
hydrated oceanic crust
(& upper mantle)
oc. mantle
c. mantle
VE 1:1
-74
-73
-72
aseismic
Paleo
lower crust (?)
Seismogenic
zone
Locally
serpentinized
mantle (?)
Asthenospheric
wedge